Band structure of *n*- and *p*-doped core-shell nanowires

Andrea Vezzosi,[1,2,*] Andrea Bertoni,[2,†] and Guido Goldoni[1,2,‡]

[1]*Dipartimento di Scienze Fisiche, Informatiche e Matematiche, Università di Modena e Reggio Emilia, Via Campi 213/a, 41125 Modena, Italy*

[2]*Centro S3, CNR-Istituto Nanoscienze, Via Campi 213/a, 41125 Modena, Italy*

(Received 3 February 2022; revised 20 April 2022; accepted 25 May 2022; published 9 June 2022; corrected 4 August 2022)

We investigate the electronic band structure of modulation-doped GaAs/AlGaAs core-shell nanowires for both *n* and *p* doping. We developed an 8-band Burt-Foreman $\mathbf{k}\cdot\mathbf{p}$ Hamiltonian approach to describe coupled conduction and valence bands in heterostructured nanowires of arbitrary composition, growth directions, and doping. Coulomb interactions with the electron/hole gas are taken into account within a mean-field self-consistent approach. We map the ensuing multiband envelope function and Poisson equations to optimized, nonuniform real-space grids by the finite element method. Self-consistent charge-density, single-particle subbands, density of states, and absorption spectra are obtained at different doping regimes. For *n*-doped samples, the large restructuring of the electron gas for increasing doping results in the formation of quasi-one-dimensional electron channels at the core-shell interface. Strong heavy-hole (HH)/light-hole (LH) coupling of hole states leads to nonparabolic dispersions with mass inversion, similarly to planar structures, which persist at large dopings, giving rise to direct LH and indirect HH gaps. In *p*-doped samples the hole gas forms an almost isotropic, ringlike cloud for a large range of doping. Here as a result of the increasing localization, HH and LH states uncouple, and mass inversion takes place at a threshold density. A similar evolution is obtained at fixed doping as a function of temperature. We show that signatures of the evolution of the band structure can be singled out in the anisotropy of linearly polarized optical absorption.

DOI: 10.1103/PhysRevB.105.245303

I. INTRODUCTION

Among III–V compound semiconductor nanostructures, radially heterostructured nanowires represent an increasingly investigated, silicon-compatible perspective for applications in transistor-based electronic devices [1] and optoelectronic devices [2,3]. From the point of view of material quality, several issues have already been settled on the route to technological exploitation of nanowires or as a platform for coherent quantum phenomena. These include self-assisted growth [4,5], order and polytypism [6,7], high-quality interfaces [8], and multilayer growth [9]. One critical issue bridging material science and device nanofabrication is the control of doping, for example, in modulation doped heterostructures [10,11] and radial *p*-*n* junctions [12]. This is still a concern in terms of reproducibility between nanowires and homogeneity within each nanowire [13,14].

As in the realm of planar heterostructures, GaAs-based nanomaterials play a special role also for nanowires. Ultra-high-mobility devices in planar GaAs/AlGaAs heterojunctions build on the modulation doping concept [15], whereby dopants are incorporated in a higher-gap AlGaAs layer, physically separated from the lower-gap layers where carriers are confined, suppressing carrier-ionized impurity scattering. A corresponding modulation doped radial heterostructure is schematically shown in Fig. 1 [10], which can be seen as a planar heterojunction with wraparound layers. Carriers are confined in the GaAs core, while dopants are incorporated in an outer AlGaAs layer. Typically, a thin GaAs capping layer is included to prevent Al oxidation. While mobility is still improving in planar systems [16], where background impurities are the limiting factor, high mobility is more difficult to achieve in core-multishell nanowires though [11,17], and experimental and theoretical characterization is needed.

Due to comparable kinetic and Coulomb energies, in doped core-shell nanowires (CSNWs), electronic states [18] and ensuing response functions [19,20] are determined by the self-consistent field of free carriers, which in turn depends on the concentration and type of doping [18] together with the Fermi-level pinning at surface states [21,22]. Hence different doping regimes may result in distinct charge localization patterns [23]. The ability to predict the band structure in doped CSNWs is, therefore, a complex task.

Among the methods used, the envelope function approach stands out for its versatility and computational efficiency. Single-band descriptions have been widely used, including nonperturbative electric and magnetic fields [18,24–26]. Multiband $\mathbf{k}\cdot\mathbf{p}$ descriptions, which include spin-orbit coupling arising from valence states that are crucial to describe, e.g., optical properties [27,28], have been employed for several classes of materials, taking into account composition modulations, crystallographic details and mesoscopic symmetries [29–35]. Spin-orbit coupling in the conduction band has been evaluated also in presence of strong magnetic fields [36–38]. However, a full description of the band structure

*andrea.vezzosi@unimore.it
†andrea.bertoni@nano.cnr.it
‡guido.goldoni@unimore.it

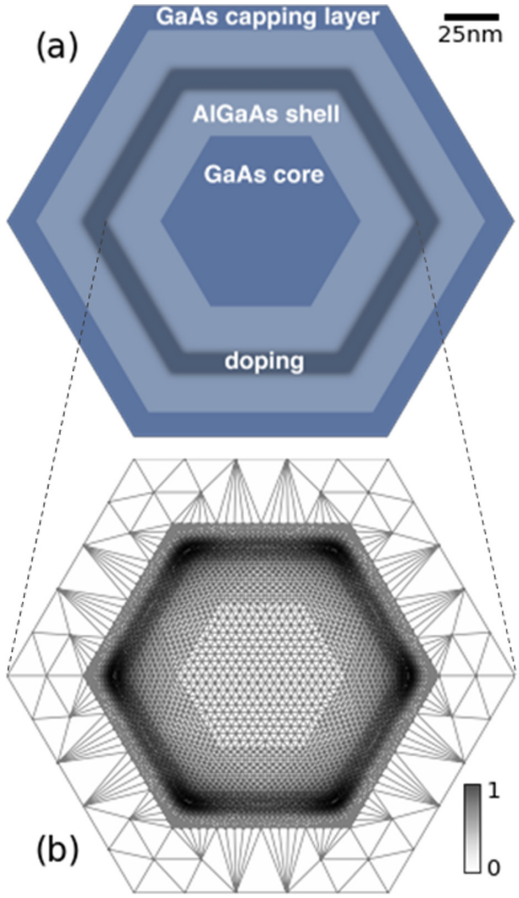

FIG. 1. (a) Sketch of the section of the simulated CSNWs. The principal axes of the 2D-coordinate system are directed along the $[11\bar{2}]$ and $[\bar{1}10]$ crystallographic directions. (b) An example of an optimized FEM grid used to solve the envelope function equation (2) with superimposed self-consistent charge density (in gray scale arbitrary units). The grid stops at the doping layer, where the charge density is assumed to vanish. The grid used for the Poisson equation is different and extends to the outer boundary of the structure.

of doped CSNWs in the different doping regimes including the self-consistent field arising from the free charge is still missing.

In this paper we investigate the electronic band structure of modulation-doped GaAs/AlGaAs CSNWs with *n*- or *p*-type doping. We employ an 8-band Burt-Foreman $\mathbf{k}\cdot\mathbf{p}$ Hamiltonian approach, with Coulomb interactions with the electron/hole gas taken into account within a mean-field self-consistent approach. The numerical burden arising from the self-consistent solution of multiband envelope function and Poisson equations is minimized by the use of the finite element method (FEM) with nonuniform real-space grids, optimized to different doping regimes. Self-consistent charge-density, single-particle subbands, density of states, and absorption spectra are then obtained. For strong *n* doping, a quasi-one-dimensional (1D) channel tends to form at the corners of the core-shell interface. Heavy-hole (HH)/light-hole (LH) couplings lead to nonparabolic dispersions with mass inversion in the valence band, similarly to planar structures, giving rise to direct LH and indirect HH gaps persisting at any doping density. In strongly *p*-doped samples, on the contrary, the hole gas forms an almost isotropic, ringlike cloud. As a result of the increasing localization, HH and LH states uncouple, and mass inversion takes place at a threshold density. Similar evolutions are obtained at fixed doping as a function of temperature. We suggest that signatures of the evolution of band structure can be traced in the anisotropy of linearly polarized optical absorption.

In Sec. II we outline our theoretical-computational methods, with detailed derivations reported in the Appendix. Emphasis is on the generality of the method and mapping on optimized FEM grids. Band structures, density of states, projected charge densities, and optical anisotropy are discussed in Sec. III as a function of the doping density, separately for both *n*- and *p*-doped samples.

II. THEORETICAL AND COMPUTATIONAL METHODS

A. The k · p description

To obtain the band structure of a modulation-doped CSNW, we have developed an 8-band $\mathbf{k}\cdot\mathbf{p}$ envelope function approach. Assuming translational invariance along the nanowire growth axis z and the position vector $\mathbf{r} = (\mathbf{r}_\perp, z)$, the nth eigenstate at the in-wire wave-vector k_z is written as

$$\Psi_n(\mathbf{r}, k_z) = \sum_{\nu=1}^{8} e^{ik_z z}\psi_n^\nu(\mathbf{r}_\perp, k_z)u^\nu(\mathbf{r}), \tag{1}$$

where $u^\nu(\mathbf{r}) = |J, J_z\rangle$ is a Bloch basis function in the total angular momentum representation [see Eq. (A18)]. We choose the quantization axis of $\mathbf{J}$ parallel to z. The coefficients $\psi_n^\nu(\mathbf{r}_\perp, k_z)$ are the νth component of the nth solution of the multiband envelope-function equation

$$\sum_{\nu=1}^{8}\left[\hat{H}_{BF}^{\mu\nu}(\mathbf{r}_\perp, k_z) - eV_{el}(\mathbf{r}_\perp)\delta^{\mu\nu}\right]\psi_n^\nu(\mathbf{r}_\perp, k_z) = E_n(k_z)\psi_n^\mu(\mathbf{r}_\perp, k_z), \tag{2}$$

where $\hat{H}_{BF}$ is the 8×8 Burt-Foreman Hamiltonian operator, with material-dependent parameters and including the band offsets, and V_{el} represents the electrostatic potential generated by free carriers and fully ionized dopants.

The operator $\hat{H}_{BF}$ is obtained from the $\mathbf{k}\cdot\mathbf{p}$ bulk Hamiltonian by replacing k_x and k_y with the corresponding differential operators. Material modulations are included by keeping track of the correct nonsymmetrized operator ordering, as described in Appendix A. This procedure yields a set of second-order coupled partial differential equations which we numerically solve using FEM on an appropriate 2D grid [39–41] with Dirichlet boundary conditions. The strongly nonparabolic subbands $E_n(k_z)$ and the corresponding envelope functions $\psi_n^\nu(\mathbf{r}_\perp, k_z)$ are finally determined on a uniform grid of wave vectors $k_z \in [-k_M, k_M]$.

From the solutions of Eq. (2), we evaluate the total charge density

$$\rho(\mathbf{r}_\perp) = e[n_h(\mathbf{r}_\perp) - n_e(\mathbf{r}_\perp) + n_D(\mathbf{r}_\perp) - n_A(\mathbf{r}_\perp)] \tag{3}$$

from the fully ionized donor or acceptor profiles, $n_D(\mathbf{r}_\perp)$ or $n_A(\mathbf{r}_\perp)$, respectively, and the free-electron and hole charge

densities given by, respectively,

$$n_e(\mathbf{r}_\perp) = \sum_{n\in \text{c.s.}} \sum_{\nu=1}^{8} \int_{-k_M}^{k_M} \frac{dk}{2\pi} f(E_n(k), \mu, T) \left|\psi_n^\nu(\mathbf{r}_\perp, k)\right|^2, \tag{4}$$

$$n_h(\mathbf{r}_\perp) = \sum_{n\in \text{v.s.}} \sum_{\nu=1}^{8} \int_{-k_M}^{k_M} \frac{dk}{2\pi} [1 - f(E_n(k), \mu, T)] \left|\psi_n^\nu(\mathbf{r}_\perp, k)\right|^2, \tag{5}$$

where the first summation runs over the conduction (valence) subband indices for electrons (holes). Here $f(E, \mu, T)$ is the Fermi-Dirac distribution function, μ is the chemical potential, T is the temperature, and k_B is the Boltzmann constant.

In practice, Eq. (2) needs to be solved only in $[0, k_M]$, since eigenstates at negative wave vectors can be obtained (up to an arbitrary phase factor) applying the time-reversal symmetry operator

$$\mathcal{T} = e^{-i\pi J_y} K, \tag{6}$$

where J_y is the y component of the total angular momentum and K is the complex conjugate operator.

The electrostatic potential $V_{el}(\mathbf{r}_\perp)$ is the solution of the Poisson equation with the source term given by the total charge density of the system, possibly with a material and position-dependent relative dielectric constant,

$$\nabla\epsilon(\mathbf{r}_\perp)\nabla V_{el}(\mathbf{r}_\perp) = -\frac{\rho(\mathbf{r}_\perp)}{\epsilon_0}. \tag{7}$$

Again, Eq. (7) is solved using FEM on a 2D grid with Dirichlet boundary conditions. The potential at the outer boundary of the CSNW is fixed to zero at the six edges of the outer layer of the structure. Note that the computational protocol allows to include arbitrary voltages at gates surrounding the nanowire [42], although we will not investigate this configuration here.

The steps described above are iterated self-consistently until convergence in a seemingly Schrödinger-Poisson cycle, here generalized to a multiband Hamiltonian. We stop iterations when the relative change of the charge density between two successive iterations falls below 10^{-3} at any node of the grid.

To characterize band states, a k_z-dependent spinorial analysis is useful. The contribution of any of the component of the envelope function can be estimated as

$$C_n^\nu(k_z) = \int \left|\psi_n^\nu(\mathbf{r}_\perp, k_z)\right|^2 \mathrm{d}\mathbf{r}_\perp, \tag{8}$$

with the normalization condition

$$\sum_{\nu=1}^{8} C_n^\nu(k_z) = 1$$

at each subband index n and wave-vector k_z. When analyzing electronic states, we shall classify states in terms of EL, HH, and LH characters [see Appendix A, Eq. (A18)], which are computed as

$$\begin{aligned} C_{\text{EL}}(k_z) &= C_n^1(k_z) + C_n^2(k_z), \\ C_{\text{HH}}(k_z) &= C_n^3(k_z) + C_n^4(k_z), \\ C_{\text{LH}}(k_z) &= C_n^5(k_z) + C_n^6(k_z). \end{aligned} \tag{9}$$

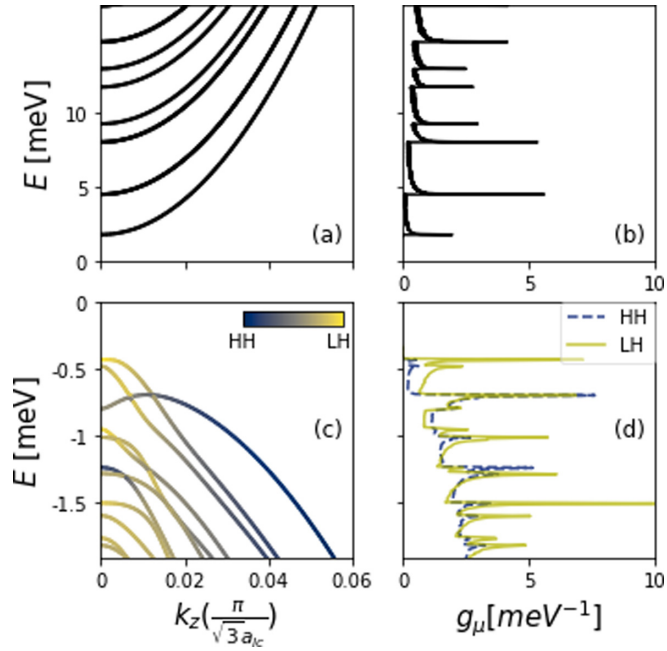

FIG. 2. Conduction (a) and valence (c) subbands of an undoped GaAs/AlGaAs CSNW (see text for parameters). In (c) the hue/color represents the spinorial character in terms of HH and LH according to Eq. (9). Conduction (b) and valence (d) PDOS for different spinor components. The zero of the energy in each panel is taken at the bulk band edge of GaAs for conduction and valence band, respectively.

We shall also plot the projected probability distributions at $k_z = 0$ defined as

$$\begin{aligned} \phi_{\text{EL}}(\mathbf{r}_\perp) &= \sum_{\nu\in\{1,2\}} C_n^\nu(0) \frac{\left|\psi_n^\nu(\mathbf{r}_\perp, 0)\right|^2}{\xi_n^\nu}, \\ \phi_{\text{HH}}(\mathbf{r}_\perp) &= \sum_{\nu\in\{3,4\}} C_n^\nu(0) \frac{\left|\psi_n^\nu(\mathbf{r}_\perp, 0)\right|^2}{\xi_n^\nu}, \\ \phi_{\text{LH}}(\mathbf{r}_\perp) &= \sum_{\nu\in\{5,6\}} C_n^\nu(0) \frac{\left|\psi_n^\nu(\mathbf{r}_\perp, 0)\right|^2}{\xi_n^\nu}, \end{aligned} \tag{10}$$

where

$$\xi_n^\nu = \max_{\mathbf{r}_\perp} \left|\psi_n^\nu(\mathbf{r}_\perp, 0)\right|^2.$$

Additionally, we compute the projected density of states (PDOS) for any given component ν of the wave function,

$$g_\nu(E) = \frac{1}{N} \sum_{n}^{\text{subbands}} \sum_{k} C_n^\nu(k) \delta(E - E_n(k)), \tag{11}$$

where N is the total number of points in k space considered in the summation. Furthermore, for n/p-doped samples we evaluate the self-consistent linear charge density of electrons/holes as

$$\rho_{\text{lin}} = \int n_{e/h}(\mathbf{r}_\perp) \mathrm{d}\mathbf{r}_\perp. \tag{12}$$

The calculation of the optical anisotropy proceeds as follows. In the dipole approximation, the interband absorption

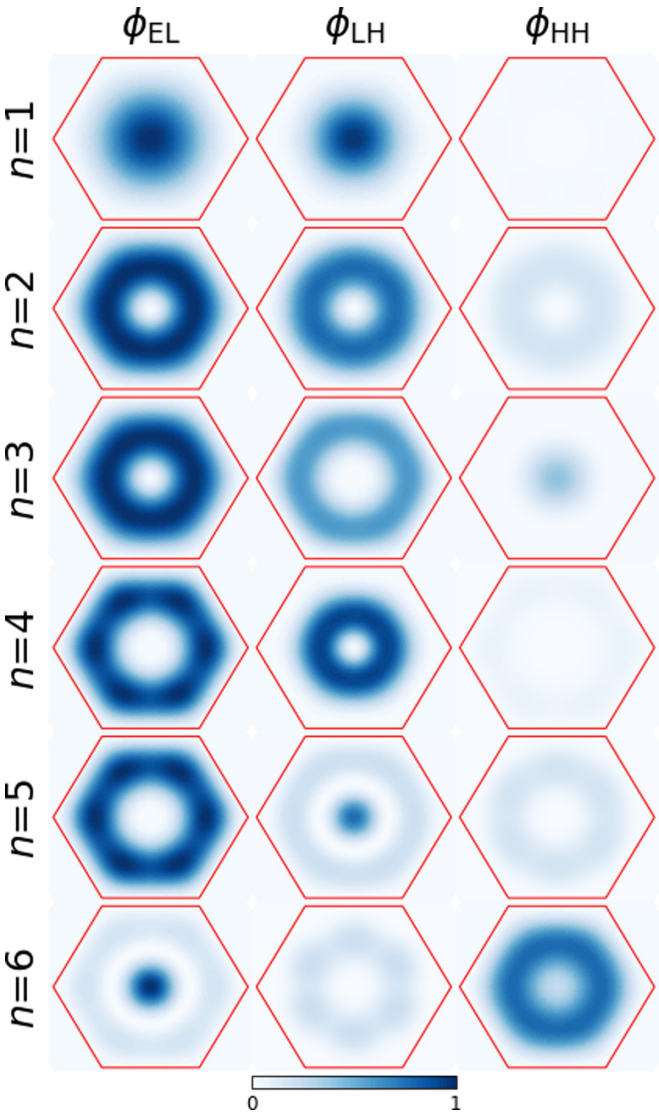

FIG. 3. Projected probability distributions [Eq. (10)] of the six lowest conduction-band (first column) and six highest valence-band states (second and third column) at Γ for the undoped material of Fig. 2.

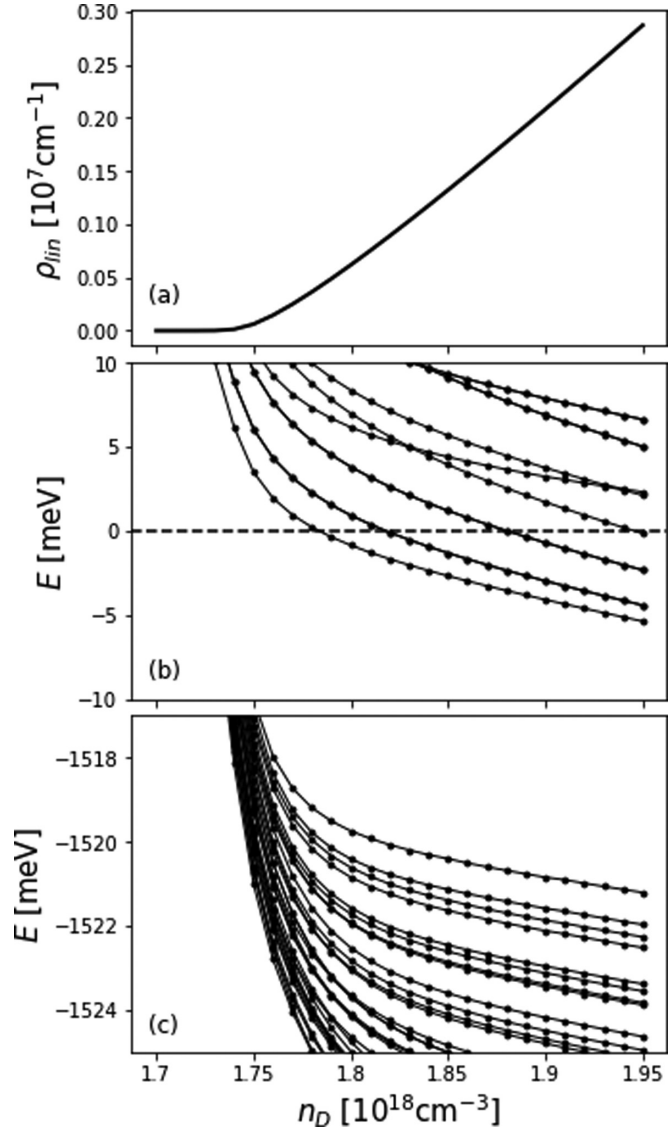

FIG. 4. (a) Linear free charge density [Eq. (12)], (b) conduction subband energies at $k_z = 0$, and (c) valence subband energies at $k_z = 0$ as a function of the doping density n_D. Energies are referred to the Fermi level.

intensity of photons with energy $\hbar\omega$ and light polarization vector $\boldsymbol{\varepsilon}$ reads:

$$I_{\boldsymbol{\varepsilon}}(\hbar\omega) \propto \sum_{n\in\text{v.s.}} \sum_{m\in\text{c.s.}} \sum_{k} \left|M^{\boldsymbol{\varepsilon}}_{n\to m,k}\right|^2 \times \left[f(E_n(k)) - f(E_m(k))\right] \delta(E_m(k) - E_n(k) + \hbar\omega), \tag{13}$$

where $M^{\boldsymbol{\varepsilon}}_{n\to m,k}$ is the interband optical matrix element [45],

$$M^{\boldsymbol{\varepsilon}}_{n\to m,k_z} \simeq \sum_{\mu\nu=1}^{8} \langle u^\mu|\boldsymbol{\varepsilon}\cdot\mathbf{p}|u^\nu\rangle \int \mathrm{d}\mathbf{r}_\perp \psi^{\mu *}_m(\mathbf{r}_\perp, k_z)\psi^\nu_n(\mathbf{r}_\perp, k_z). \tag{14}$$

Note that doping, in addition to determine the envelope functions via the self-consistent field, enters Eq. (13) through Fermi-Dirac distributions, which accounts for band filling effects when electron/hole subband edges approach the Fermi energy due to doping. For undoped structures, the Fermi energy is well within the gap, and this term is almost equal to unity. In heavily doped structures, however, it inhibits interband transitions to the lowest subbands which may be nonnegligibly occupied.

Finally, we compute the relative optical anisotropy β between linearly polarized light along the wire axis, I_{ε_z} and perpendicular to it along the x direction, I_{ε_x},

$$\beta = \frac{I_{\varepsilon_z} - I_{\varepsilon_x}}{I_{\varepsilon_z} + I_{\varepsilon_x}}. \tag{15}$$

B. Numerical implementation details

The above self-consistent 8-band $\mathbf{k}\cdot\mathbf{p}$ equations may result in a computationally intensive task, but a number of strategies can be implemented to keep the computational

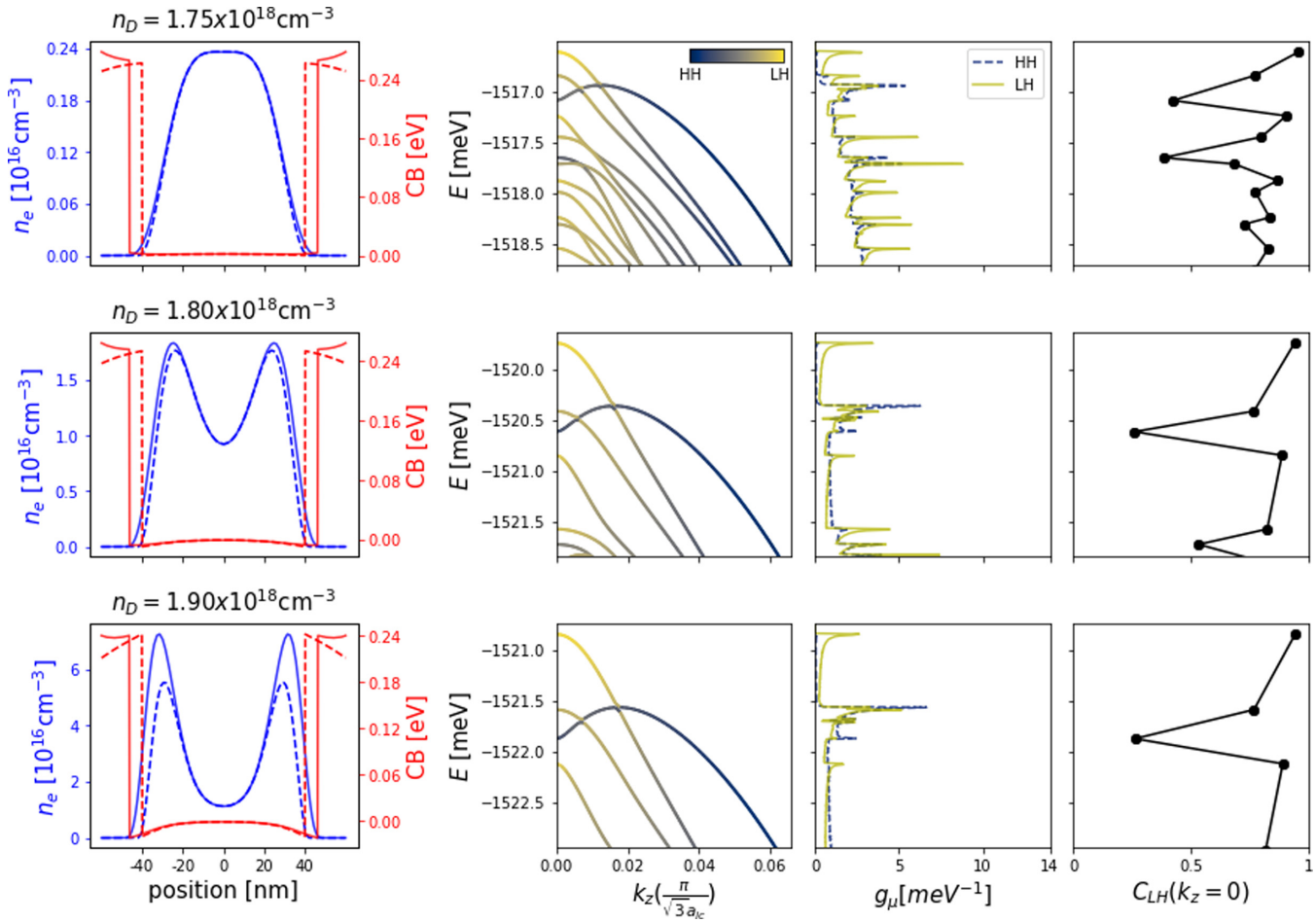

FIG. 5. Left column: Free charge-density distribution n_e (blue) and self-consistent conduction-band profile CB (red) shown along the edge-to-edge (dashed line) and corner-to-corner (full line) directions of the CSNW section for $T = 20$ K at selected values of n_D, as indicated. Doping increases from top to bottom. Middle left and middle right columns: Valence subbands and PDOS, respectively, corresponding to the doping density and self-consistent potential of the left panels. The hue/color represents the spinorial character in terms of HH and LH according to Eq. (9). Right column: LH character of each subband at Γ.

burden low and avoid the use of massively parallel architectures. Most of the strategies mentioned below take advantage of the flexibility of FEM which allows the use of nonuniform grids, which we generate by the `Free FEM` library [46].

The $\mathbf{k}\cdot\mathbf{p}$ Hamiltonian is represented on a 2D hexagonal domain, partitioned in a D_6 symmetry-compliant, unstructured mesh of triangular elements. Since at different doping levels the charge density forms substantially dissimilar localization patterns [18], different density-optimized grids are used at different doping levels. A typical grid used for a high density regime is shown in Fig. 1(b), showing that the grid is denser where the charge density is localized.

We emphasize that the use of the centrosymmetric grid is critical to correctly reproduce the expected degeneracies without the need of extremely dense grids. Breaking the inversion symmetry of the grid would not only artificially split the orbital degeneracy expected in the conduction band (see Sec. III A) but also split the spin degeneracy, particularly in the strongly spin-orbit coupled valence band [47]. The need to maintain the inversion symmetry discourages the use of automatic adaptive grid methods. Hence we use fixed, although optimized, nonuniform grids.

In CSNWs which are at stage here, the charge density is confined to the GaAs core (although in a nontrivial manner) and rapidly goes to zero inside the shell material; therefore, we use larger elements inside the shell with respect to the core and we require the envelope function to vanish somewhere inside the shell, typically at the doping layer. A typical grid used in the calculations is shown in Fig. 1(b). Finally, we found it convenient to use coarser grids during the self-consistent cycle, with the optimized, finer grid used only in the last iterations.

For the 8-band $\mathbf{k}\cdot\mathbf{p}$ model, the bound states of interest around the gap correspond to interior eigenvalues of the Hamiltonian matrix. To compute the charge density via Eqs. (4) and (5), the sum is restricted to a few tens of subbands (usually $n_{\max} = 60$ for the electrons and $n_{\max} = 100$ for holes), and iterative methods are preferable. We use the Arnoldi method [48], implemented in the `ARPACK` library [49], together with the shift-and-invert approach, where the original problem is recast to target the largest eigenvalues. This approach provides faster convergence and enables the search for $n_{\max}$ eigenvalues around an energy value E_{search}. Thus since for both n and p doping the occupation of the minority carrier is negligible, during the self-consistent cycle one needs to

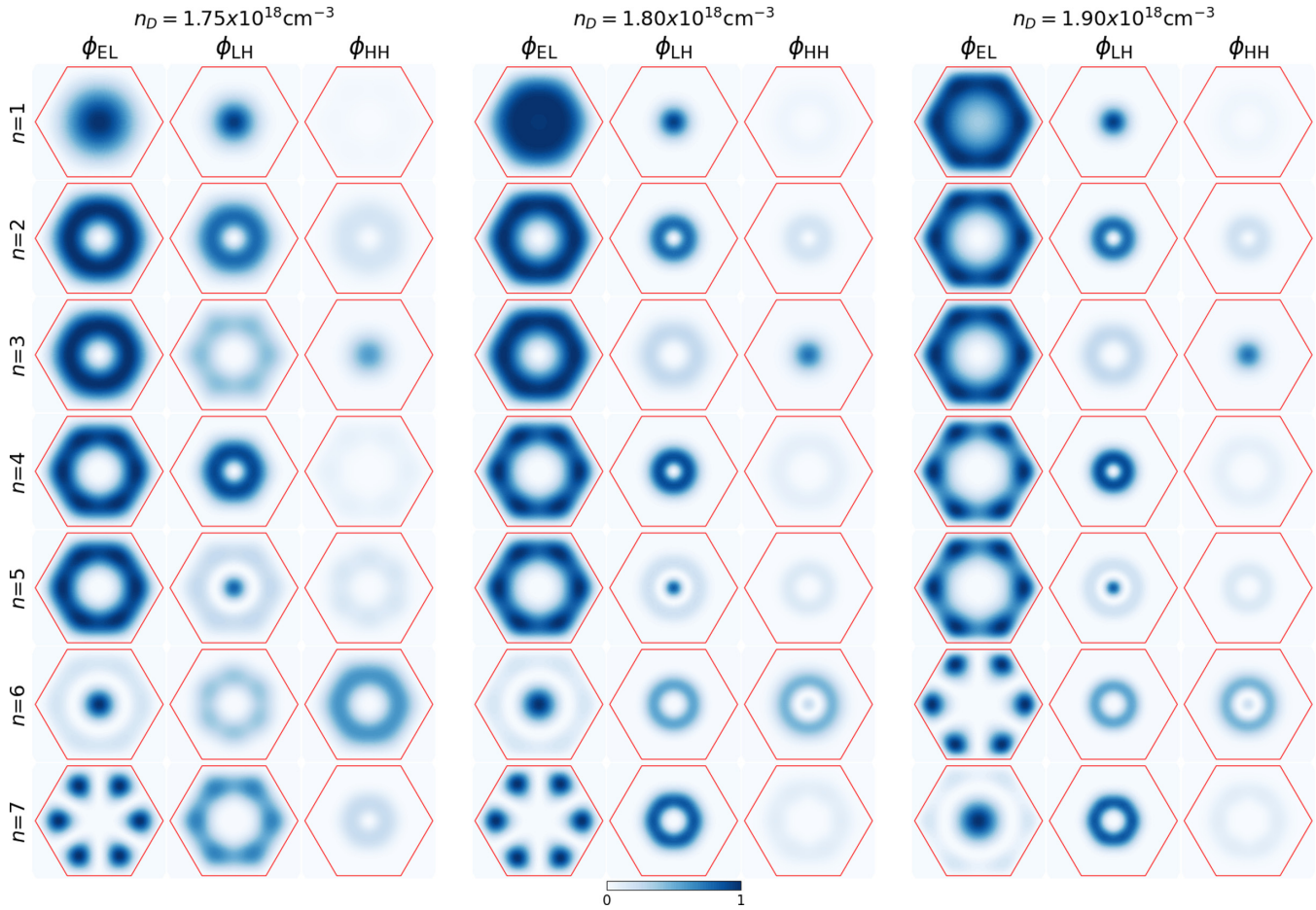

FIG. 6. Projected probability distributions [Eq. (10)] for the seven lowest conduction and seven highest valence subbands at the same selected doping densities of Fig. 5, as indicated. Each column corresponds to the EL, LH, and HH components, as indicated.

solve only for the conduction or the valence-band structure, respectively, by properly choosing E_{search} [50]. The full band structure is then calculated only in the final converged self-consistent potential.

The Poisson equation is solved on a single specific mesh extending over the entire 2D domain of the heterostructure. To go back-and-forth between the grids of the envelope function and Poisson solver, as well as between different grids used during the self-consistent cycle, we make use of 2D linear interpolation. To achieve the convergence of the self-consistent protocol we rely on the modified second Broyden's method [51–54] when updating the electrostatic potential at the current iteration. The inverse Jacobian is updated using the information from $M = 8$ previous iterations. We fixed the weight corresponding to the first iteration to $w_0 = 0.01$, while all the other weights w_m, with $m = 1, ..., M - 1$, are computed as suggested in Ref. [52]. The simple mixing parameter α is fixed to 0.05.

Before the simulation starts, the mesh is processed through a bandwidth reduction procedure leveraging the reverse Cuthill–McKee algorithm [55] implemented within the `SciPy` library [56]. This is done in order to obtain tightly banded sparse matrices from the FEM discretization.

The above self-consistent numerical protocol and ancillary calculations have been implemented in a `Python` library. A typical run uses a grid of about 7000 triangular elements and 3500 nodes for the $\mathbf{k} \cdot \mathbf{p}$ problem and 10–20 self-consistent iterations. A run on a single node architecture equipped with 16 2.60 GHz Intel Xeon E5-2670 processor cores takes about 6 h CPU time.

III. RESULTS

We simulate a typical modulation-doped structure [11] consisting of a GaAs hexagonal core with an edge-to-edge distance of 80 nm surrounded by a 50-nm-wide $Al_{0.3}Ga_{0.7}As$ shell and a GaAs capping layer of thickness 10 nm [see Fig. 1(a)]. The 2D-coordinate system has the x and y axes directed along the $[11\bar{2}]$ and $[\bar{1}10]$ crystallographic directions, respectively. Buried inside the shell, at a distance of 20 nm from the core-shell interface, a 10-nm-thick layer is doped at a constant density n_D of donors or n_A of acceptors. All calculations discussed below are performed at $T = 20$ K, except in Sec. III D. The chemical potential μ is fixed at the midgap value of GaAs [22].

A. Band structure of the undoped material

As a reference for calculations of the band structure of doped CSNWs to be discussed in the next sections, we first

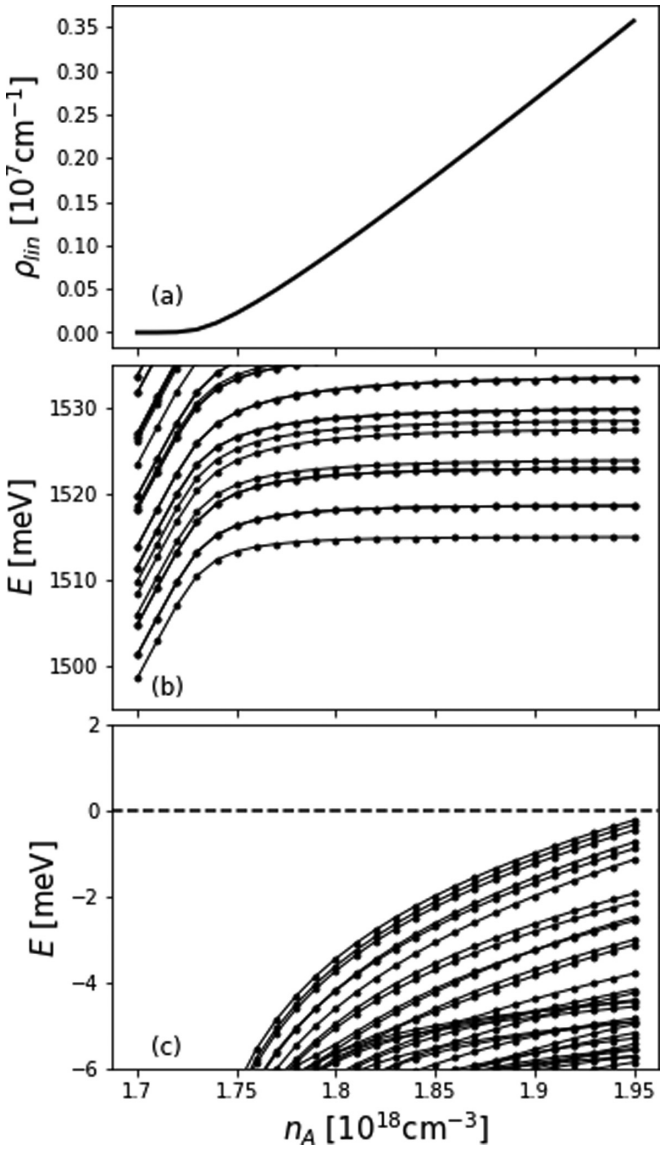

FIG. 7. (a) Linear free charge density [Eq. (12)], (b) conduction subband energies at $k_z = 0$, and (c) valence subband energies at $k_z = 0$ as a function of the doping density n_A. Energies are referred to the Fermi level.

consider an undoped sample and analyze the conduction and valence-band subbands, which are shown in Fig. 2 (left), together with the corresponding PDOSs (right). These are best analyzed together with the projected probability distributions of the EL, HH, and LH spinor components [see Eqs. (9) and (10)] at $k_z = 0$, which are shown separately in Fig. 3 [57].

We first consider conduction states. Due to the large gap of GaAs, which disentangles conduction and valence bands in the $\mathbf{k}\cdot\mathbf{p}$ Hamiltonian, conduction subbands [Fig. 2(a)] show an almost pure EL character with parabolic dispersion and ensuing $1/\sqrt{\text{energy}}$ PDOS [Fig. 2(b)]. In a system with D_{6h} symmetry, assuming a perfectly isotropic band structure, we expect the ground state to be nondegenerate, while the second/third and fourth/fifth doublets are degenerate [58]. Here anisotropic residual interactions with the valence band remove the degeneracies by $\sim 10^{-3}$meV, a quantity that cannot be distinguished in Fig. 2. Indeed, the single/double degeneracy of the levels is easily recognized in the height of the peaks of the PDOS.

As shown in Fig. 3 (left column), the lowest conduction state is $1s$-like in the center, while the nearly degenerate doublets are ringlike states with an increasing modulation in the corners of the hexagonal confining potential. The 6th state is again a nondegenerate state with a $2s$ character. Higher levels (not shown here) have maxima on the corners of the hexagon and nodes along the facets or vice versa [58,59].

The valence subbands [Fig. 2(c)] are, of course, denser in energy than conduction subbands due to the larger mass of holes. The LH-HH mixing, which is small but finite also at Γ, leads to a strongly nonparabolic dispersion of the subbands with k_z. As shown by the color code of the lines, the two highest subbands have a predominant LH character at Γ, which is also shown by the corresponding distribution functions in Fig. 3 (center and right columns) [60]. In between several subbands in Fig. 2(c) pointing downward and with a strong LH character at Γ, we recognize a mixed character state (the third subband) and an almost HH subband (the 6th state) (see also Fig. 3). These two subbands strongly couple at finite wave vectors (note from the hue that these two subbands exchange their HH-LH character), causing a strong camel's back dispersion of the third subband and a corresponding peak in the PDOS at ~ -0.54 meV with 50% character of either HH or LH components. All in all, the LH character dominates the PDOS, which agrees with Ref. [33]. Note that band crossings of the third subband can be traced to states belonging to different irreducible representations of the C_{3v} double symmetry group of [111] oriented nanowires with hexagonal cross-section [61–63].

The probability distributions of HH and LH states shown in Fig. 3 are either s-like or ringlike (arising from a quadrupolar symmetry of the real/imaginary parts of the envelope functions), similarly to corresponding conduction states, although, of course, the ordering is different, as HH- and LH-like states interlace. No orbital degeneracies are expected, since the strongly anisotropic bulk valence-band structure does not share the hexagonal symmetry of the confinement.

We finally note that all electronic states are doubly spin-degenerate due to the centro-symmetric symmetry of the system (which is carefully preserved by the FEM grid), which will hold true in all calculations throughout [64].

B. *n* Doping

We now consider n-doped samples with increasing doping density n_D up to high-doping regimes. As shown in Fig. 4(a), the self-consistent linear charge density [Eq. (12)] increases almost linearly for large doping, while an increasing number of conduction subbands fall below the Fermi energy [Fig. 4(b)]. The evolution of the (unoccupied) valence-band states at Γ is also shown in Fig. 4(c).

The evolution of the localization of the self-consistent charge density and the corresponding electrostatic potential, shown in Fig. 5 (left), is not trivial. With increasing doping, the charge density evolves from a small, isotropic charge distribution in the core of the structure to a larger, ringlike charge-density distribution and finally to a charge density which is primarily located in the corners of the core, as can be inferred by comparing the edge-to-edge and corner-to-corner

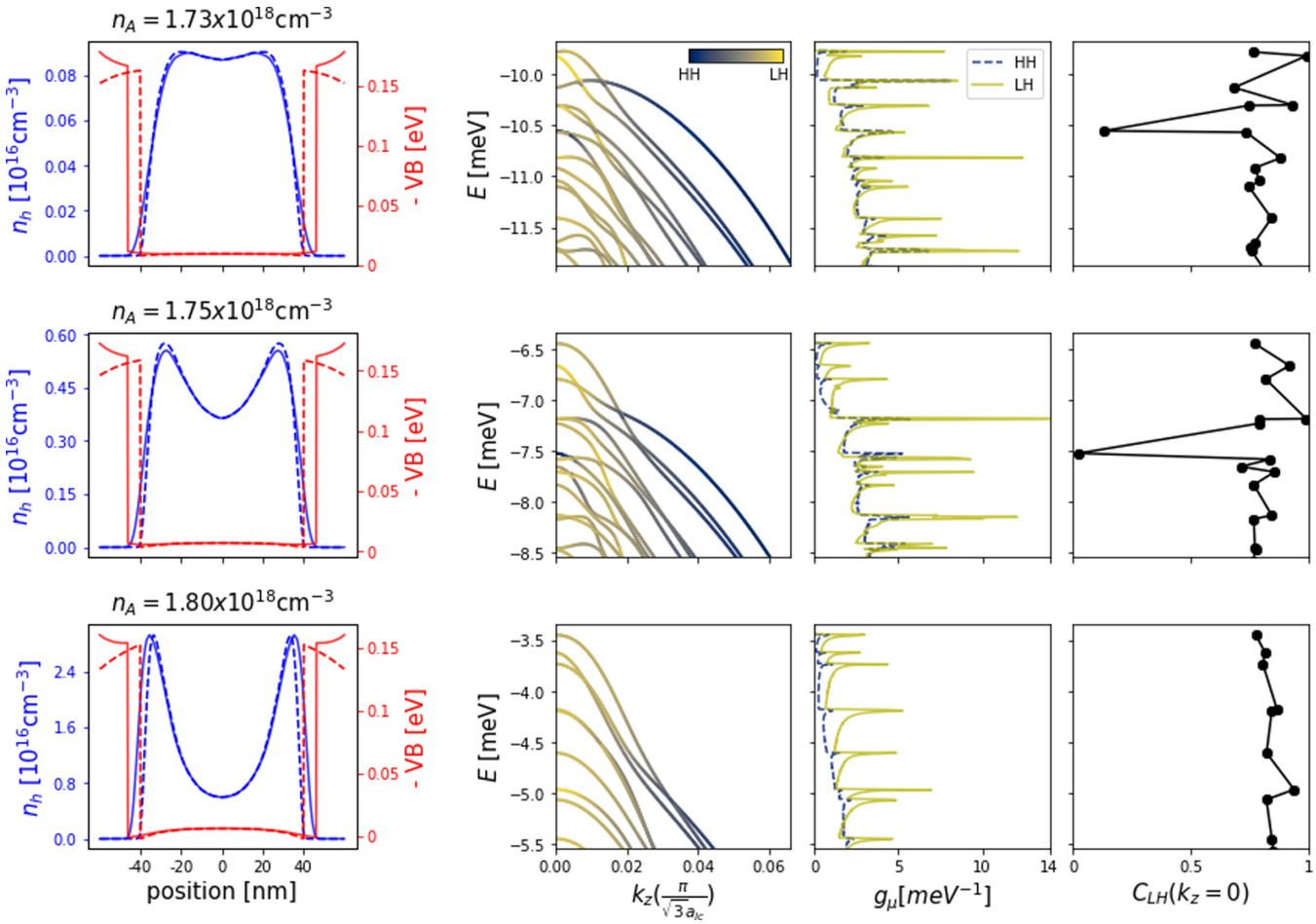

FIG. 8. Left column: Free charge-density distribution n_h (blue) and self-consistent valence-band profile VB (red) shown along the edge-to-edge (dashed line) and corner-to-corner (full line) directions of the CSNW section for $T = 20$ K at selected values of n_A, as indicated. Doping increases from top to bottom. Middle left and middle right columns: Valence subbands and PDOS, respectively, corresponding to the doping density and self-consistent potential of the left panels. The hue/color represents the spinorial character in terms of HH and LH, according to Eq. (9). Right column: LH character of each subband at Γ.

profiles in Fig. 5. This is in agreement with single-band self-consistent calculations [18,65], as expected from the nearly pure EL character of conduction subbands.

Conduction subbands retain a trivial parabolic dispersion regardless of the doping level (and type), which is therefore not shown here. However, it is still interesting to consider the evolution of the localization of the conduction envelope functions shown in terms of the projected density distribution $\phi_{\rm EL}(\mathbf{r}_\perp)$ in Fig. 6 (left columns in each panel), with increasing doping (panels from left to right). For each of the seven lowest levels, the larger the doping the more localized is $\phi_{\rm EL}(\mathbf{r}_\perp)$ at the core-shell interface. For the largest doping shown here, all subbands feature a clear sixfold symmetry induced by the heterostructure confining potential. Note that the ordering of the levels in terms of symmetry depends on the level of doping, as seen from the "exchange" of the 6th and 7th levels with increasing doping.

Although for n doping the charge density is determined by conduction-band states, the valence-band structure does have an evolution as well due to the restructuring of the free charge density and ensuing change in the self-consistent confining electrostatic potential shown in Fig. 5. The valence-band structure shown in Fig. 5 (second column) shows a downward shift of the subbands and an increase of the intersubband gaps due to the increased localization energy at the core-shell interface. The $k_z = 0$ character (Fig. 5, right column) at low doping is $\sim 10 \div 30\%$ LH for most states, except for the ground level which is almost completely LH and two states which stand out with a strong HH character. Increasing doping increases the gaps but does not change much the subband dispersions. At the largest doping shown here, the PDOS is dominated by (i) a LH peak near the gap and (ii) two overlapping peaks, one arising from a LH band and one from a HH band. Note, however, that the latter HH peak arises from the camel's back subband with a maximum at a finite k_z and, therefore, an indirect gap with the conduction band.

Figure 6 shows that as doping increases holes tend to be more localized in the center, with a mostly isotropic distribution. This differs from conduction states which move toward the GaAs/AlGaAs interface at larger doping densities, and it is due to the opposite sign of the electrostatic energy. Note that, as already noted for EL states, also for HH and LH states,

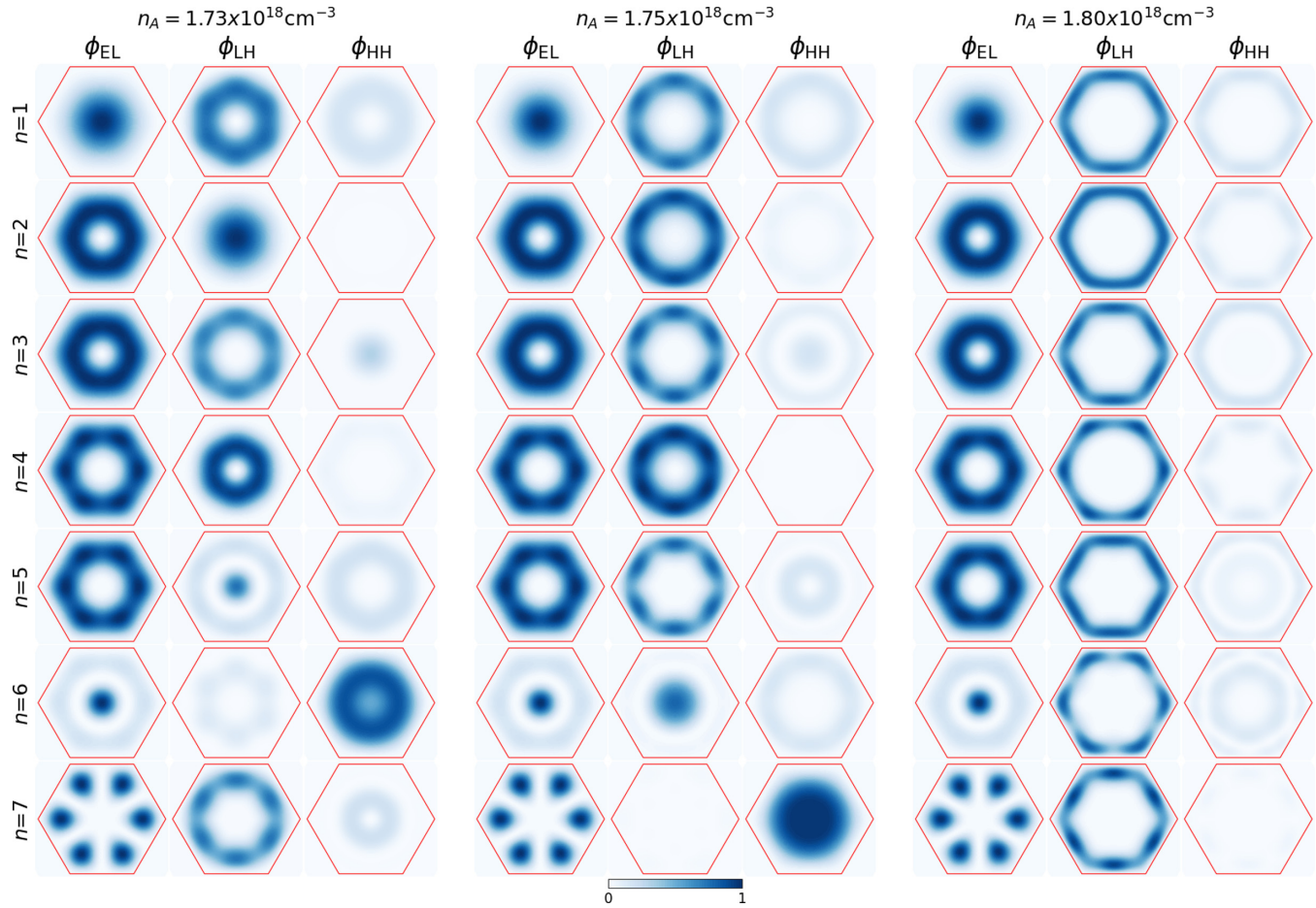

FIG. 9. Projected probability distributions [Eq. (10)] for the seven lowest conduction and seven highest valence subbands at the same selected doping densities of Fig. 8, as indicated. Each column corresponds to the EL, LH, HH component, as indicated.

the order in terms of symmetry is not preserved as doping is swept. For example the 7th level changes both character and orbital symmetry as n_D moves from 1.75 to 1.80 10^{18} cm^{-3}.

C. *p* Doping

We next discuss the results for p-doped materials, focusing on the effects of an increasing acceptor density n_A on the band structure and the hole charge-density localization.

Figure 7 shows a linear increase of the free charge density after a threshold density of dopants. Note that the range of densities is similar with respect to the n-doping case despite the very different parameters and, as we shall see below, charge localization.

Indeed, the free charge n_h, shown in Fig. 8 (left) at selected values of the acceptor density n_A, shows a dip in the center already at weak doping, which is consistent with the larger mass and a lower confinement energy of holes with respect to conduction electrons. As the acceptor doping density n_A increases, the charge progressively moves toward the interfaces to minimize Coulomb energy, analogous to the n-doping case. However, different from the latter case, the hole gas remains remarkably isotropic, as seen by comparing the edge-to-edge and corner-to-corner profiles which nearly coincide in Fig. 8 (left). In other words, the hole charge forms a uniform gas with a cylindrical shape and little resemblance to the host hexagonal confining potential up to these doping densities.

As n_A is swept, the conduction levels [Fig. 7(b)] shift in energy with respect to the Fermi level and finally stabilize, while an increasing number of hole subbands approach the Fermi energy and contribute to the free charge. Note that at large dopings, hole levels separate in a low-energy and a high-energy branch, which correspond to increasingly LH- and HH-like levels, respectively.

At difference with the n-doping case, the hole band structure is strongly affected by p doping, as exemplified in Fig. 8. This is due to the different localization energies of HHs and LHs in the increasingly localizing self-consistent potential. A prominent effect can be seen by comparing Figs. 8 and 9. The only strongly HH level (the 6th level in Fig. 9, left panel) moves to lower energy due to the light mass. As a result, HH-LH mixing and related anticrossings are removed, the mass of the camel's back subband changes sign, and all bands point downward with a small mass at the large densities. Note that the PDOS at large doping is dominated by far by LH states. Furthermore, as a consequence of the reduced $\mathbf{k} \cdot \mathbf{p}$ coupling in the valence band at high doping densities, the hole energy levels at Γ tend to group in sixfold clusters [see Fig. 7(c)] separated by gaps that increase with increasing n_A [58].

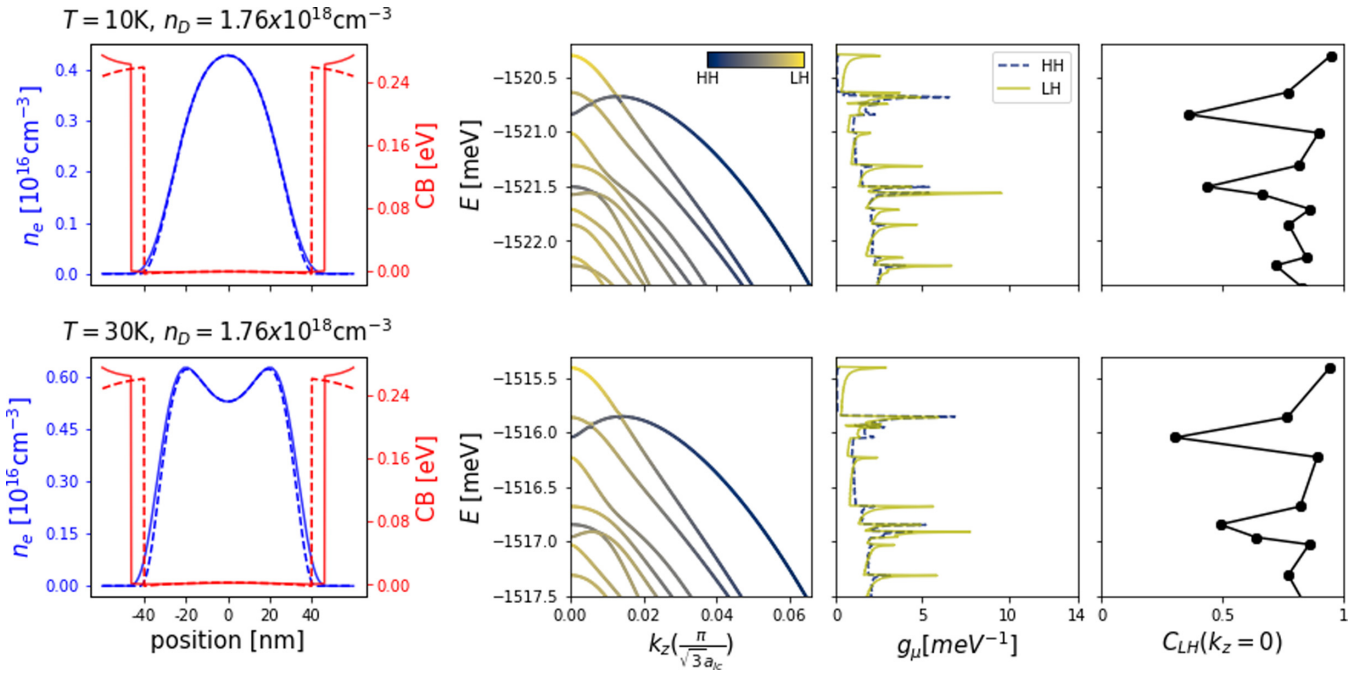

FIG. 10. Left column: Free charge-density distribution n_e (blue) and self-consistent conduction-band profile CB (red) shown along the edge-to-edge (dashed line) and corner-to-corner (full line) directions of the CSNW section for $T = 10$ K (top row) and $T = 30$ K (bottom row) at the single doping density $n_D = 1.76 \times 10^{18}$ cm^{-3}. Middle left and middle right columns: Valence subbands and PDOS, respectively, corresponding to the doping density, temperature and self-consistent potential of the left panels. The hue/color represents the spinorial character in terms of HH and LH, according to Eq. (9). Right column: LH character of each subband at Γ.

Figure 9 shows that all highest valence subbands become strongly localized at the interfaces at high doping. Contrary to conduction electrons, however, which always tend to localize at the six corners, holes alternate subbands localized at the corners and at the facets, which is again in agreement with single-band calculations in Ref. [18]. Since the charge density is a convolution of these levels, the isotropy of the hole cloud noted above is justified.

We also note that, as doping is increased, there is no definite order of LH- and HH-like levels in term of symmetry/localization due to the increasing hole confinement energy toward the core-shell interface which is different for HH and LH components.

Finally, we note that, similarly to *n*-doped samples, minority carriers localize in the opposite direction due to the opposite sign of the self-consistent potential. However, conduction electrons are much more rigid and stable due to the light mass hence showing little evolution with doping density, and in particular no symmetry inversion takes place.

D. Temperature dependence

The electronic states discussed above are the result of the competition between comparable energy scales in the meV range. As temperatures of ∼10 K are in the same energy range, we expect that small changes in temperature at this scale may bring about strong restructuring of the electronic system. As we shall see below, in general the effect of a temperature variation on the free-carrier charge density and the valence-band structure are qualitatively analogous to the effects of a varying doping density.

In Fig. 10 we consider an *n*-doped sample with donor density $n_D = 1.76 \times 10^{18}$ cm^{-3} at $T = 10$ K (top row) and $T = 30$ K (bottom row), which are above and below the temperature used in Sec. III B. Such temperature variations, respectively, increase or decrease the bulk band-gap values of 1 meV with respect to the values in Table I for both the

TABLE I. Material parameters used in the simulations at $T = 20$ K. E_g is the energy gap; ΔE_c, ΔE_v are the conduction and valence-band offset values at the GaAs/$Al_{0.3}Ga_{0.7}As$ interface; Δ_{so} is the split-off energy; E_p is the bare Kane energy; $E_p^{\rm rsc}$ the rescaled Kane energy [Eq. (A6)]; m_e is the effective conduction electron mass; γ_i are the bare Luttinger parameters; $\tilde{\gamma}_i$ are the rescaled values [Eq. (A9)]; ϵ_r is the relative dielectric constant; and a_{lc} is the lattice constant. The band-structure parameters are taken from Ref. [43] except for the band offset values. The latter have been determined assuming an offset ratio of $\Delta E_c : \Delta E_v = 63 : 37$, as recommended in Ref. [44]

	GaAs		$Al_{0.3}$/ $Ga_{0.7}$/As
E_g [eV]	1.518		1.936
ΔE_c [eV]		0.263	
ΔE_v [eV]		0.155	
Δ_{so} [eV]	0.341		0.323
$E_p/E_p^{\rm rsc}$ [eV]	28.8 / 20.9		26.5 / 18.0
m_e	0.067		0.092
$\gamma_1/\tilde{\gamma}_1$	6.98 / 2.39		6.01 / 2.91
$\gamma_2/\tilde{\gamma}_2$	2.06 / −0.235		1.69 / 0.138
$\gamma_3/\tilde{\gamma}_3$	2.93 / 0.635		2.48 / 0.928
ϵ_r	13.18		12.24
a_{lc} [nm]	0.56		

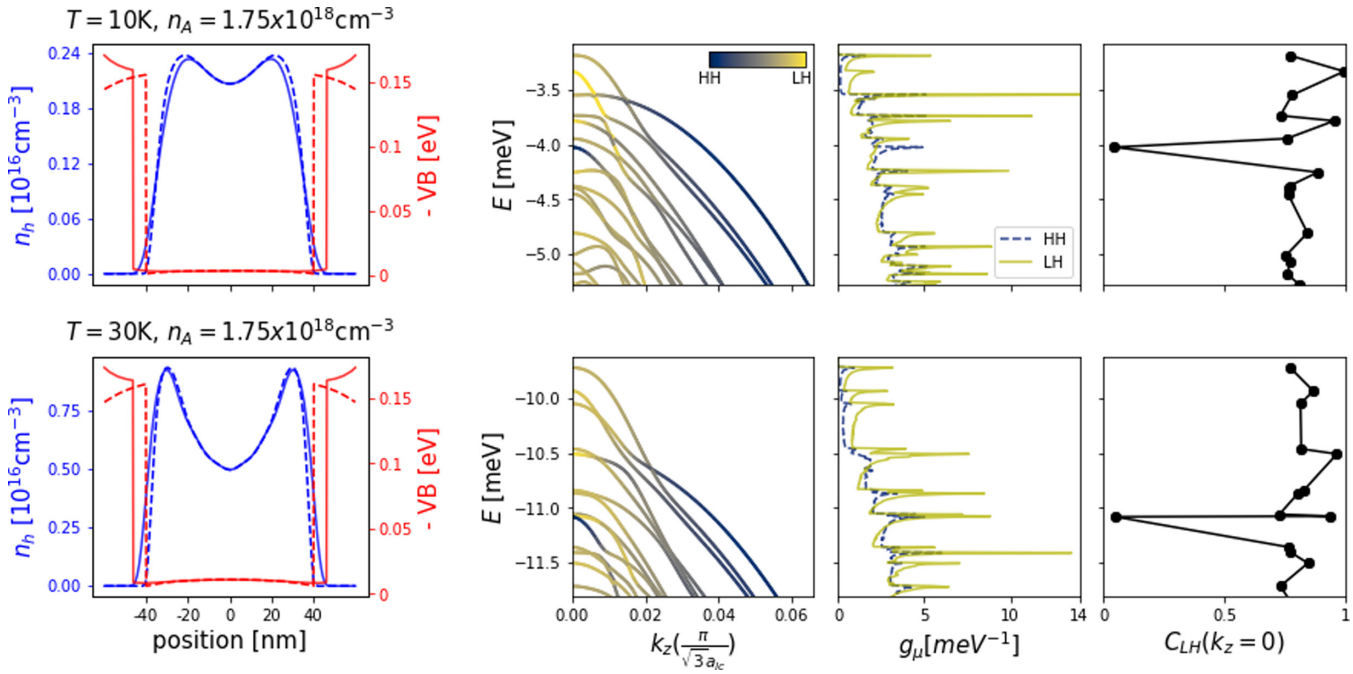

FIG. 11. Left column: Free charge-density distribution n_h (blue) and self-consistent valence-band profile VB (red) shown along the edge-to-edge (dashed line) and corner-to-corner (full line) directions of the CSNW section for $T = 10$ K (top row) and $T = 30$ K (bottom row) at the single doping density $n_A = 1.75 \times 10^{18}$ cm^{-3}. Middle left and middle right columns: Valence subbands and PDOS, respectively, corresponding to the doping density, temperature, and self-consistent potential of the left panels. The hue/color represents the spinorial character in terms of HH and LH, according to Eq. (9). Right column: LH character of each subband at Γ.

core and the shell materials. As a result, the band offsets are unchanged, while the band-structure parameters that are affected by a rescaling procedure are slightly modified. Starting at the lower temperature, the electronic charge density (left column) evolves from an isotropic charge density centered in the core to a ringlike density. This is similar to the effect of increasing doping, as in Fig. 5, as the occupation probability of the levels above the chemical potential increases with temperature and more charge populates the nanowire. Consistent with Fig. 5, the valence-band structure and PDOS are little affected by temperature in this range. However, the subbands are shifted in the opposite direction with respect to Fig. 5.

In Fig. 11 we consider a p-doped sample with acceptor density $n_A = 1.75 \times 10^{18}$cm^{-3} at the same two temperature as above. Again, increasing the temperature results in a greater hole charge density and a more pronounced charge depletion in the center due to the Coulomb interaction. Clearly, valence-band states are more sensitive to changes in the charge density for p doping. Indeed, Fig. 11 shows that as temperature is increased, HH-like states move to lower energies, while HH-like subbands change their curvature downward. As a consequence, the PDOS undergoes a substantial restructuring, as all main features are LH-like. Note that in contrast to the case of a doping density variation, the valence-band structure is shifted downward when the temperature increases.

E. Optical anisotropy

Optical absorption in quasi-1D systems is dominated by excitonic and polarization effects induced by Coulomb interactions, not included in Eqs. (13) and (14) [66,67]. However, the optical anisotropy between linearly polarized light along and transverse the nanowire axis should be less sensitive to Coulomb effects [27,28]. On the other hand, while x-polarized light couples to HH states [see Eq. (A18)], z-polarized light does not. Hence β is a sensitive probe of the orbital composition of valence-band states [27].

In Fig. 12 we show the calculated relative optical anisotropy β [Eq. (15)] at selected doping concentrations for n- (left) and p-doped (right) samples, respectively. Doping concentration increases from top to bottom in both panels. To emphasize the anisotropy of the more intense absorption peaks, the line darkness is modulated with the intensity of the absorption spectrum at the given photon energy. For reference, we also show in the inset single-particle absorption spectra in the two polarizations (for the undoped sample) with optical transitions from the nth valence state to the mth conduction state labeled $\textcircled{mn}$.

As a reference, we shall first describe the spectral anisotropy of the undoped sample [top panels in Figs. 12(a) and 12(b)]. The first positive structure, labeled $\boxed{\text{a}}$, arises from the fundamental optical transition $\textcircled{11}$ [see inset of Fig. 12(a)] which involves the almost purely LH state. This is also an intense transition due to the overlapping envelope functions components (see Fig. 3, first row). The positive anisotropy is $\beta \simeq 3/5$, which is expected from the ratio between the momentum matrix element in the z and x directions,

$$\left|\left\langle S, \pm\tfrac{1}{2}\middle|p_z\middle|\tfrac{3}{2}, \pm\tfrac{1}{2}\right\rangle\right|^2 = 4\left|\left\langle S, \pm\tfrac{1}{2}\middle|p_x\middle|\tfrac{3}{2}, \pm\tfrac{1}{2}\right\rangle\right|^2,$$

hence $\beta = \frac{4-1}{4+1}$.

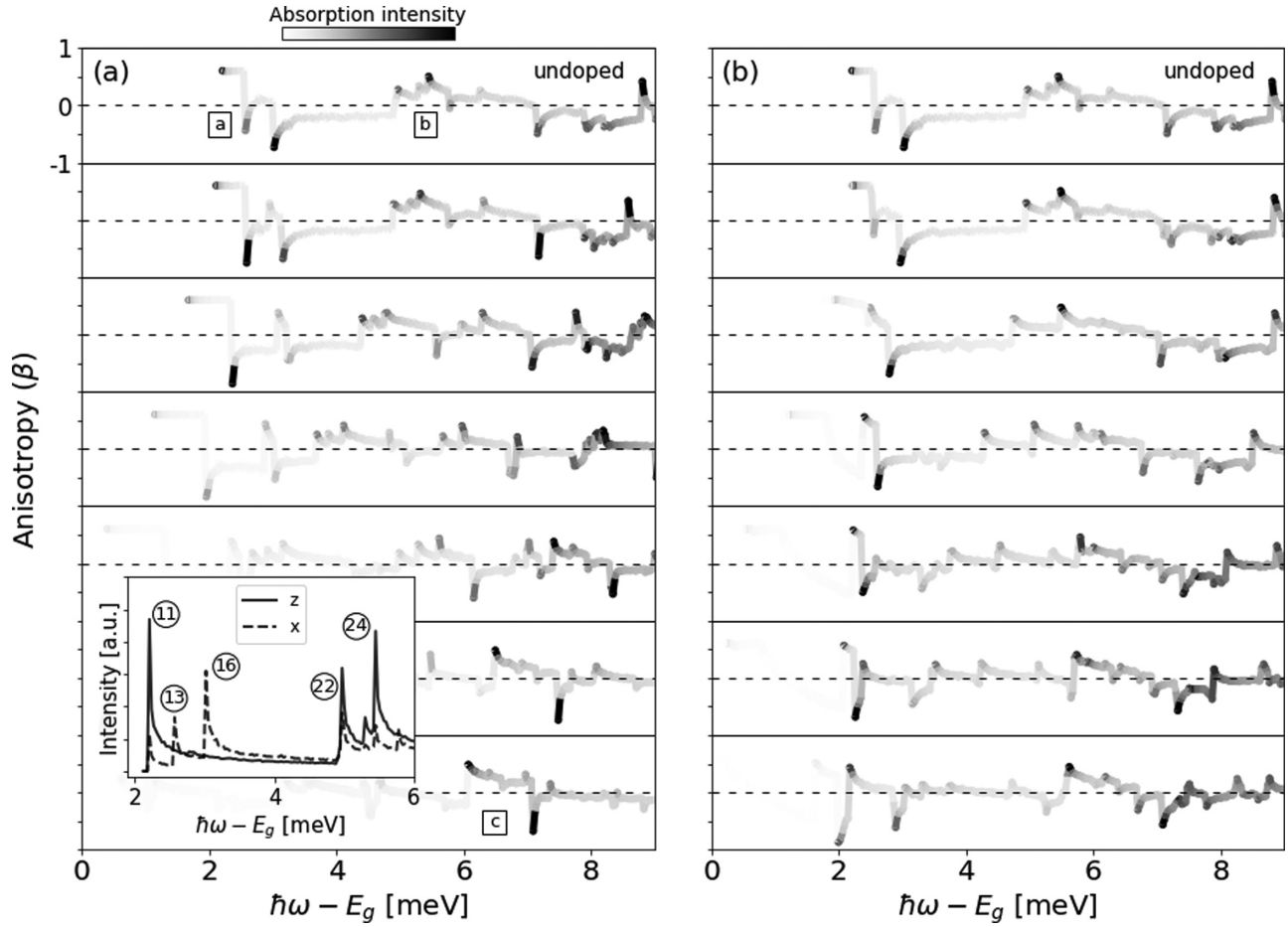

FIG. 12. (a) Optical anisotropy β [Eq. (15)] for n-doped samples at different donor concentrations. From top to bottom: Undoped, 1.75, 1.77, 1.79, 1.82, 1.87, 1.90 $\times 10^{18}$ cm^{-3}. Horizontal dashed lines indicate the zero reference; each panel extends vertically from -1 to $+1$. The gray hue represents the intensity of the corresponding absorption spectrum [Eq. (13)] at the given photon energy. $E_g = 1.518$ eV is the band gap of GaAs at $T = 20$ K. Inset: Calculated absorption spectra of the undoped structure for linearly polarized light. Peaks are labeled with (*mn*), where m is the index of the final conduction subband and n is the index of the initial valence subband involved in the optical transition. (b) Same as panel (a) but for p-doped samples. From top to bottom: Undoped, 1.73, 1.75, 1.77, 1.79, 1.80, 1.82 $\times 10^{18}$ cm^{-3}.

The next two negative dips in the anisotropy structure a involve the $m = 1$ EL subband and arise from the HH components of transitions (13) and (16) (see Fig. 3, third and sixth rows). As HH components do not couple to EL states for light linearly polarized along z, we indeed expect the anisotropy to be negative for these optical transitions.

A second, positive anisotropy set of structures at higher photon energies, labeled b, involves transitions to the $m = 2$ conduction subband with predominantly LH initial states, namely, (22) and (24) transitions (see also Fig. 3, second and fourth rows).

As the optical anisotropy discriminates specific transitions, it is interesting to discuss how the anisotropy spectra evolve with doping concentration. As seen in Figs. 12(a) and 12(b) in both n- and p-doped samples, the absorption edge experiences a red-shift with increasing doping due to band-gap renormalization. In Fig. 13 we compare the energy difference ΔE between the ground-state energy of the conduction and the valence band, respectively, showing that the effective energy gap decreases almost linearly for both kinds of samples in the range of a few meV as doping concentration rises.

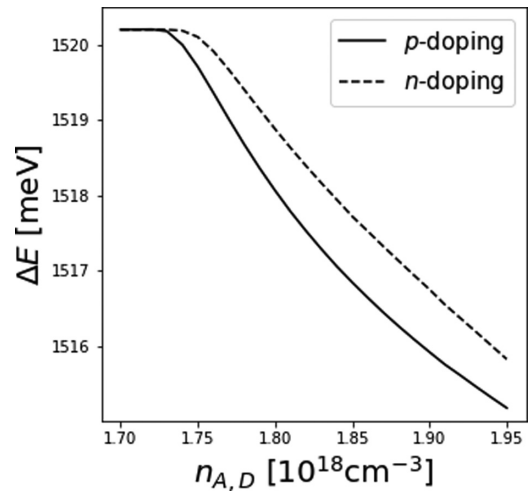

FIG. 13. Effective energy-gap ΔE as a function of doping concentration for n- and p-doped samples.

In n-doped samples, Fig. 12(a), the absorption intensity of the lowest transitions gradually vanishes with doping, which is due to two concomitant effects, (i) band filling due to electron subbands falling below the Fermi level, which inhibits interband absorption to these levels, and (ii) optical matrix element reduction, which is due to Coulomb repulsion; the free charge distribution in the occupied band tends to localize toward the core-shell interfaces as doping concentration is increased while confining states in the center in the other band, lessening the optical matrix element between initial and final states [Eq. (14)]. Both effects contribute to suppress low-energy absorption at high-doping, finally moving the absorption edge to the strongly anisotropic structure [c] originated by transitions to the $m = 7$ EL subband, namely, (71) mainly LH with positive anisotropy, and (73) mainly HH, hence with negative anisotropy.

For p-doped samples, see Fig. 12(b), the band-filling effect is less pronounced within the examined range of doping. In fact, even at the highest acceptor density shown in Fig. 12(b), the highest valence subband does not cross the Fermi level (see Fig. 7). Here the suppression of the absorption intensity with positive anisotropy at [a] is mainly due to reduction of the initial and the final states' overlap due to an increasing localization toward the core-shell interfaces of the hole ground-state envelope function (see Fig. 9, first row). The first negative dip gradually disappears because the third valence subband loses its HH character with increasing doping (see Fig. 9, third row and Fig. 8, second column). The opposite occurs for the second negative anisotropy peak, which persists at high doping due to the increasing HH character of the sixth hole subband with doping, as already pointed out in Sec. III C, which in turn increases the optical matrix element for x-polarized light.

IV. CONCLUSIONS

We have thoroughly investigated the band structure of doped GaAs-based CSNWs, with an emphasis on the evolution of spin-orbit coupled valence-band states with doping of either n or p type. This is an important piece of information for the characterization of such materials where doping is still an issue.

Our calculations, performed with a state-of-the-art Burt-Foreman 8-band $\mathbf{k}\cdot\mathbf{p}$ description, treat many-body effects at the mean-field level and extend previous investigations to realistic descriptions of doped materials. The use of a flexible FEM approach, which allows to use nonuniform grids, proved to be numerically efficient at different doping levels. This is clearly an advantage in view of multiparameter optimization, e.g., by stochastic methods [35,68,69].

In particular, we have investigated a prototypical CSNW with remote doping. As in corresponding planar heterojunctions, the conduction subbands feature a parabolic in-wire dispersion, while hole subbands have a complex dispersion, with inverted masses, which has been rationalized in terms of HH-LH mixing. In large core nanowires, with small confinement energies, increasing doping density moves the majority carriers to the core-shell interface in order to reduce the Coulomb energy. Correspondingly, the states of the minority carrier band are confined to the core by the self-consistent electrostatic field, and in general the overlap of conduction and valence states decreases. While this is qualitatively true for both types of dopings, our calculations allow to identify several differences between the two type of samples which may have an impact, in particular, on optical absorption. In particular, for p doping the valence-band structure is strongly reshaped by confinement of holes at the core-shell interface, and all low-energy excitations have a strong LH character.

It may be expected that band structure affects optical absorption and, in particular, optical anisotropy for light polarized along or normal to the nanowire axis. Hence we have evaluated the doping density-dependent optical anisotropy, which is able to distinguish the spin-orbital character of the transition. In addition to the expected band-filling effects, specific signatures can be identified in the anisotropy patterns which distinguish between n and p doping.

ACKNOWLEDGMENTS

Discussions with Paweł Wójcik are gratefully acknowledged. A.B. acknowledges partial financial support from the EU project IQubits (Call No. H2020-FETOPEN-2018-2019-2020-01, Project ID No. 829005). The authors acknowledge CINECA for HPC computing resources and support under the ISCRA initiative (No. IsC87 ESQUDO–HP10CXQWD5).

APPENDIX A: $\mathbf{k}\cdot\mathbf{p}$ HAMILTONIAN

In this Appendix we show how to obtain the operator $\hat{H}_{BF}$ in Eq. (2). In the Cartesian basis

$$\lambda = \{|S\uparrow\rangle, |S\downarrow\rangle, |X\uparrow\rangle, |Y\uparrow\rangle, |Z\uparrow\rangle, |X\downarrow\rangle, |Y\downarrow\rangle, |Z\downarrow\rangle\}, \tag{A1}$$

the Burt-Foreman Hamiltonian with the principal axis along the [001] direction can be written as

$$H^{\lambda} = H_0 + V + H_{so}. \tag{A2}$$

The $\mathbf{k}\cdot\mathbf{p}$ Hamiltonian H_0, neglecting bulk inversion asymmetry terms, is given by [70]

$$H_0 = \begin{pmatrix} \mathbf{k}^{\mathrm{T}}A_c\mathbf{k} & 0 & iP\mathbf{k}^{\mathrm{T}} & \mathbf{0}^{\mathrm{T}} \\ 0 & \mathbf{k}^{T}A_c\mathbf{k} & \mathbf{0}^{\mathrm{T}} & iP\mathbf{k}^{\mathrm{T}} \\ -i\mathbf{k}P & \mathbf{0} & H_v & \mathbf{0}_{3\times3} \\ \mathbf{0} & -i\mathbf{k}P & \mathbf{0}_{3\times3} & H_v \end{pmatrix} \tag{A3}$$

where $\mathbf{k} = (k_x, k_y, k_z)^{\mathrm{T}}$, P is the optical matrix parameter related the the Kane energy parameter by

$$P = \sqrt{\frac{\hbar^2}{2m_0}E_p}, \tag{A4}$$

and A_c is the renormalized conduction-band effective mass parameter,

$$A_c = \frac{\hbar^2}{2m_e} - \frac{2}{3}\frac{P^2}{E_g} - \frac{1}{3}\frac{P^2}{E_g + \Delta_{so}}. \tag{A5}$$

For many relevant semiconductors, including the present case, the standard parameters lead to a negative value for A_c. This fact induces spurious solutions [71] that bend within the band gap for large wave vectors. To avoid these unphysical results, we set $A_c = \frac{\hbar^2}{m_0}$ and rescale the E_p parameter in order to still

get the correct conduction-band dispersion [72,73]

$$E_p^{\text{rsc}} = \frac{E_g(E_g+\Delta_{so})}{E_g+\frac{2}{3}\Delta_{so}}\left(\frac{m_0}{m_e}-2\right). \tag{A6}$$

Foreman rigorously showed that this approach is not an approximation and is equivalent to a change of the Bloch basis [74]. We checked that for the regimes investigated and with the relatively coarse grids permitted by the use of FEM, no highly oscillatory, discretization-related spurious solutions appears in our calculations [71].

In the above expression the matrix H_v reads

$$H_v = \frac{\hbar^2\mathbf{k}^2}{2m_0}\mathbb{I}_{3\times3} + \begin{pmatrix} k_xLk_x+k_yMk_y+k_zMk_z & k_xN^+k_y+k_yN^-k_x & k_xN^+k_z+k_zN^-k_x \\ k_yN^+k_x+k_xN^-k_y & k_xMk_x+k_yLk_y+k_zMk_z & k_yN^+k_z+k_zN^-k_y \\ k_zN^+k_x+k_xN^-k_z & k_zN^+k_y+k_yN^-k_z & k_xMk_x+k_yMk_y+k_zLk_z \end{pmatrix}, \tag{A7}$$

where L, M, N^+, and N^- are the Dresselhaus-Kip-Kittel parameters which read

$$\begin{aligned} L &= \frac{\hbar^2}{2m_0}(-\tilde{\gamma}_1-4\tilde{\gamma}_2-1), \\ M &= \frac{\hbar^2}{2m_0}(2\tilde{\gamma}_2-\tilde{\gamma}_1-1), \\ N^+ &= \frac{\hbar^2}{2m_0}[-6\tilde{\gamma}_3-(2\tilde{\gamma}_2-\tilde{\gamma}_1-1)], \\ N^- &= \frac{\hbar^2}{2m_0}(2\tilde{\gamma}_2-\tilde{\gamma}_1-1). \end{aligned} \tag{A8}$$

Here the modified Luttinger parameters $\tilde{\gamma}_i$ are

$$\begin{aligned} \tilde{\gamma}_1 &= \gamma_1 - \frac{E_p^{\text{rsc}}}{3E_g}, \\ \tilde{\gamma}_2 &= \gamma_2 - \frac{E_p^{\text{rsc}}}{6E_g}, \\ \tilde{\gamma}_3 &= \gamma_3 - \frac{E_p^{\text{rsc}}}{6E_g}, \end{aligned} \tag{A9}$$

where E_g is the bulk band gap and E_p^{rsc} the rescaled Kane energy.

In Eq. (A2) the last two terms represent, respectively, the in-plane potential profile due to different band edges of adjacent layer materials

$$V = \text{diag}[E_c, E_c, \bar{E}_v, \bar{E}_v, \bar{E}_v, \bar{E}_v, \bar{E}_v, \bar{E}_v], \tag{A10}$$

with $\bar{E}_v = E_v - \frac{\Delta_{so}}{3}$, and the spin-orbit interaction Hamiltonian

$$H_{so} = \frac{\Delta_{so}}{3}\begin{pmatrix} 0&0&0&0&0&0&0&0 \\ 0&0&0&0&0&0&0&0 \\ 0&0&0&-i&0&0&0&1 \\ 0&0&i&0&0&0&0&-i \\ 0&0&0&0&0&-1&i&0 \\ 0&0&0&0&-1&0&i&0 \\ 0&0&0&0&-i&-i&0&0 \\ 0&0&1&i&0&0&0&0 \end{pmatrix}. \tag{A11}$$

The Hamiltonian H^λ can be rewritten in the form

$$H^\lambda = \sum_{\alpha,\beta=x,y,z} k_\alpha D^{\alpha\beta}k_\beta + \sum_{\alpha=x,y,z} F_L^\alpha k_\alpha + k_\alpha F_R^\alpha + G, \tag{A12}$$

where $D^{\alpha,\beta}$, $F_{L(R)}^\alpha$ and G are 8×8 matrices that can be directly obtained from Eq. (A2) by properly collecting terms involving the same powers of the wave vector's components. In particular, $D^{\alpha,\beta} \neq D^{\beta,\alpha}$ and $F_L^\alpha \neq F_R^\alpha$. It should be also noted that these matrices are not Hermitian. Nevertheless, the sums $D^{\alpha,\beta}+D^{\beta,\alpha}$ and $F_L^\alpha + F_R^\alpha$ are indeed Hermitian.

To treat nanowires oriented along an arbitrary direction we define $\mathbf{k}$ in Eq. (A12) in the rotated coordinate system. We have $\mathbf{r}' = R\,\mathbf{r}$ and $\mathbf{k}' = R\,\mathbf{k}$, where R is the orthogonal rotation matrix

$$R(\theta,\phi) = \begin{pmatrix} \cos\theta\cos\phi & \sin\phi\cos\theta & -\sin\theta \\ -\sin\phi & \cos\phi & 0 \\ \cos\phi\sin\theta & \sin\phi\sin\theta & \cos\theta \end{pmatrix}. \tag{A13}$$

The matrices in Eq. (A12), when expressed in terms of the rotated wave vector, $\mathbf{k}' = R\,\mathbf{k}$, transform according to

$$D^{\alpha\beta}(\theta,\phi) = \sum_{\alpha'\beta'} R_{\alpha\alpha'}D^{\alpha'\beta'}R^{-1}_{\beta'\beta}, \tag{A14}$$

$$F^\alpha_{L(R)}(\theta,\phi) = \sum_{\alpha'} F^{\alpha'}_{L(R)}R^{-1}_{\alpha'\alpha}, \tag{A15}$$

where $D^{\alpha\beta}$ and $F^\alpha_{L(R)}$ are the matrices defined in the original coordinate system with principal axis directed along the [001] direction. For convenience, from now on we will omit the (θ,ϕ) notation, implicitly assuming that each of the matrices $D^{\alpha\beta}$ and $F^\alpha_{L(R)}$ is defined in the rotated coordinate system.

The transformation that connects the Cartesian basis $\{\lambda\}$ to a new one with the principal axis directed along the (θ,ϕ) direction is given by $\{\gamma\} = AU\{\lambda\}$,

$$\begin{aligned} \{\gamma\} = \{&|S'\uparrow'\rangle, |S'\downarrow'\rangle, |X'\uparrow'\rangle, |Y'\uparrow'\rangle, |Z'\uparrow'\rangle, \\ &|X'\downarrow'\rangle, |Y'\downarrow'\rangle, |Z'\downarrow'\rangle\}, \end{aligned} \tag{A16}$$

where $U = \text{diag}[1,1,R,R]$ is a standard rotation operator and $A = \text{diag}[\bar{A}, \bar{A}\otimes\mathbb{I}_{3\times3}]$, where

$$\bar{A} = \begin{pmatrix} e^{-i\phi/2}\cos\theta/2 & e^{i\phi/2}\sin\theta/2 \\ -e^{-i\phi/2}\sin\theta/2 & e^{i\phi/2}\cos\theta/2 \end{pmatrix} \tag{A17}$$

rotates the spin.

We now chose the following symmetry adapted basis that diagonalizes spin-orbit interaction [75]:

$$\begin{aligned} \{\chi\} = \{&\left|\tfrac{1}{2},\tfrac{1}{2}\right\rangle_{\text{EL}} = |S'\uparrow'\rangle, \\ &\left|\tfrac{1}{2},-\tfrac{1}{2}\right\rangle_{\text{EL}} = i|S'\downarrow'\rangle, \\ &\left|\tfrac{3}{2},\tfrac{3}{2}\right\rangle_{\text{HH}} = \sqrt{1/2}|(X'+iY')\uparrow'\rangle, \end{aligned}$$

$$
\begin{aligned}
\left|\tfrac{3}{2},-\tfrac{3}{2}\right\rangle_{\mathrm{HH}} &= i\sqrt{1/2}|(X'-iY')\downarrow'\rangle,\\
\left|\tfrac{3}{2},\tfrac{1}{2}\right\rangle_{\mathrm{LH}} &= i\sqrt{1/6}|(X'+iY')\downarrow'\rangle - i\sqrt{2/3}|Z'\uparrow'\rangle,\\
\left|\tfrac{3}{2},-\tfrac{1}{2}\right\rangle_{\mathrm{LH}} &= \sqrt{1/6}|(X'-iY')\uparrow'\rangle + \sqrt{2/3}|Z'\downarrow'\rangle,\\
\left|\tfrac{1}{2},\tfrac{1}{2}\right\rangle_{\mathrm{SO}} &= \sqrt{1/3}(|(X'+iY')\downarrow'\rangle + |Z'\uparrow'\rangle),\\
\left|\tfrac{1}{2},-\tfrac{1}{2}\right\rangle_{\mathrm{SO}} &= -i\sqrt{1/3}(|(X'-iY')\uparrow'\rangle - |Z'\downarrow'\rangle)\Big\}.
\end{aligned}
\tag{A18}
$$

Note that here the total angular momentum is defined with respect to the principal axes in the rotated coordinate system. It follows that the transformation matrix to go from $\{\gamma\}$ to $\{\chi\}$ is

$$
Q = \begin{pmatrix}
1 & 0 & 0 & 0 & 0 & 0 & 0 & 0\\
0 & i & 0 & 0 & 0 & 0 & 0 & 0\\
0 & 0 & \frac{1}{\sqrt{2}} & i\frac{1}{\sqrt{2}} & 0 & 0 & 0 & 0\\
0 & 0 & 0 & 0 & 0 & i\frac{1}{\sqrt{2}} & \frac{1}{\sqrt{2}} & 0\\
0 & 0 & 0 & 0 & -i\sqrt{\frac{2}{3}} & i\frac{1}{\sqrt{6}} & -\frac{1}{\sqrt{6}} & 0\\
0 & 0 & \frac{1}{\sqrt{6}} & -i\frac{1}{\sqrt{6}} & 0 & 0 & 0 & \sqrt{\frac{2}{3}}\\
0 & 0 & 0 & 0 & \frac{1}{\sqrt{3}} & \frac{1}{\sqrt{3}} & i\frac{1}{\sqrt{3}} & 0\\
0 & 0 & -i\frac{1}{\sqrt{3}} & -\frac{1}{\sqrt{3}} & 0 & 0 & 0 & i\frac{1}{\sqrt{3}}
\end{pmatrix}.
\tag{A19}
$$

Defining $P = QAU$ to be the transformation matrix from $\{\lambda\}$ to $\{\chi\}$, the matrices in H^{λ} expressed in terms of the rotated wave-vector $\mathbf{k}'$ transform according to [33]

$$
\begin{aligned}
D^{\alpha\beta} &\to P^* D^{\alpha\beta} P^T,\\
F^{\alpha}_{L(R)} &\to P^* F^{\alpha}_{L(R)} P^T,\\
G &\to P^* G P^T.
\end{aligned}
\tag{A20}
$$

To obtain the operator $\hat{H}_{BF}$ appearing in the envelope function equations we now perform the replacements ($k_x \to -i\frac{\partial}{\partial x}$, $k_y \to -i\frac{\partial}{\partial y}$) in Eq. (A12) paying attention to preserve the correct operator ordering. Since k_z is now just a parameter, the Hamiltonian operator after the replacement has the following form

$$
\hat{H}_{BF} = \sum_{\alpha,\beta=x,y} \partial_\alpha \bar{D}^{\alpha\beta}\partial_\beta + \sum_{\alpha=x,y} \bar{F}^{\alpha}_{L}\partial_\alpha + \partial_\alpha \bar{F}^{\alpha}_{R} + \bar{G},
\tag{A21}
$$

where

$$
\begin{aligned}
\bar{D}^{\alpha\beta} &= -D^{\alpha\beta},\\
\bar{F}^{\alpha}_{L} &= -i\left(F^{\alpha}_{L} + k_z D^{z\alpha}\right),\\
\bar{F}^{\alpha}_{R} &= -i\left(F^{\alpha}_{R} + k_z D^{\alpha z}\right),\\
\bar{G} &= G + k_z^2 D^{zz} + k_z\left(F^{z}_{R} + F^{z}_{L}\right).
\end{aligned}
\tag{A22}
$$

APPENDIX B: FEM IMPLEMENTATION

Equations (2) and (7) are solved within the FEM framework [39]. Here one writes the proper action integral $\mathcal{A}$ that generates the above set of coupled differential equations through a variational procedure. For the multiband $\mathbf{k}\cdot\mathbf{p}$ equations we have [35,70]

$$
\begin{aligned}
\mathcal{A} = \sum_{\mu\nu}\int \mathrm{d}\mathbf{r}_\perp \psi^*_\mu \Bigg[&\sum_{\alpha\beta=x,y} -\overleftarrow{\partial}_\alpha \bar{D}^{\alpha\beta}_{\mu\nu}\vec{\partial}_\beta\\
&+ \sum_{\alpha=x,y}\left(\bar{F}^{\alpha}_{L,\mu\nu}\vec{\partial}_\alpha - \overleftarrow{\partial}_\alpha \bar{F}^{\alpha}_{R,\mu\nu}\right) + \bar{G}_{\mu\nu} - E\,\delta_{\mu\nu}\Bigg]\psi_\nu,
\end{aligned}
\tag{B1}
$$

where μ and ν indicate the components of the envelope function. Here the correct operator ordering is retained if we take the differential operator to act on the left (right) when $\hat{k}_{x,y}$ multiplies $F^{x,y}_{R}$ ($F^{x,y}_{L}$). It is easy to check that Eq. (B1) is equivalent to the original eigenvalue problem Eq. (2) by performing a functional variation of $\mathcal{A}$ with respect to ψ^*_μ and invoking the principle of least action. Here surface terms arising from the integration by parts can be eliminated using the continuity of the envelope function and of the probability current across the interfaces [76,77]. If the wave function is set to zero on the domain boundaries, the boundary surface term vanishes too.

The action integral $\mathcal{A}$ is discretized into n_{el} triangular finite elements of the 2D domain,

$$
\mathcal{A} = \sum_{i_{el}}^{n_{el}} \mathcal{A}^{(i_{el})}.
\tag{B2}
$$

Within the i_{el} element, each component of the unknown envelope function is approximated using Lagrange linear interpolation polynomials [40] $N_j(\mathbf{r}_\perp)$ so that

$$
\psi_\mu(\mathbf{r}_\perp) = \sum_{j=1}^{3} \psi_{\mu j} N_j(\mathbf{r}_\perp),
\tag{B3}
$$

where the expansion coefficients $\psi_{\mu j}$ represent the value of the μ-th component of the envelope function at the j-th triangle's vertex, also called nodal point.

Using Eqs. (B1) and (B3), we obtain

$$
\begin{aligned}
\mathcal{A}^{(i_{el})} &= \sum_{\mu\nu}\sum_{ij=1}^{3} \psi^*_{\mu i}\left[\int d\mathbf{r}_\perp N_i(\mathbf{r}_\perp)\mathcal{L}_{\mu\nu} N_j(\mathbf{r}_\perp)\right]\psi_{\nu j}\\
&= \sum_{\mu\nu}\sum_{ij=1}^{3} \psi^*_{\mu i}\mathcal{M}^{(i_{el})}_{\mu\nu ij}\psi_{\nu j},
\end{aligned}
\tag{B4}
$$

where $\mathcal{L}_{\mu\nu}$ represents the operators appearing in the integrand of Eq. (B1), namely, the Lagrangian density.

The total action is given by the sum of each element's contribution. This can be written in a very natural manner in matrix form by imposing interelement continuity through carefully overlaying the element matrices $\mathcal{M}^{(i_{el})}$ [39]. To understand how to construct a global matrix starting from element matrices it is convenient to make a simple example. Let us consider a single component of the envelope function $\psi_\mu = \psi$ and two adjacent triangular elements ($i_{el} = 1, 2$) having two nodes (and one edge) in common. The action integral for these two elements reads

$$
\mathcal{A} = \sum_{ij=1}^{3} \psi^{(1)*}_i \mathcal{M}^{(1)}_{ij}\psi^{(1)}_j + \sum_{ij=1}^{3} \psi^{(2)*}_i \mathcal{M}^{(2)}_{ij}\psi^{(2)}_j.
\tag{B5}
$$

Since the two elements share two nodes and we require interelement continuity, we set $\psi_1^{(1)} = \psi_1^{(2)}$, $\psi_2^{(1)} = \psi_2^{(2)}$, where it is implicitly assumed that the first and the second node of both elements, respectively, overlap. Using the above conditions, it is possible to rewrite Eq. (B5) in the *global* form

$$\mathcal{A} = \sum_{IJ=1}^{4} \psi_I^* \mathcal{M}_{IJ} \psi_J, \tag{B6}$$

where I and J now stand for global node indices and $\mathcal{M}$ is obtained from $\mathcal{M}^{(1)}$ and $\mathcal{M}^{(2)}$ by summing the contributions from the same nodes and collecting the envelope functions on common vertices, e.g., for $I, J = 1, 2$ we have $\mathcal{M}_{IJ} = \mathcal{M}_{IJ}^{(1)} + \mathcal{M}_{IJ}^{(2)}$.

From this example it is now easy to see that the action integral in its global form can be written as

$$\mathcal{A} = \sum_{\mu\nu} \sum_{IJ}^{n_{\text{glob}}} \psi_{\mu I}^* \mathcal{M}_{\mu\nu IJ} \psi_{\nu J}, \tag{B7}$$

where n_{glob} is the total number of nodes on the discretization domain. We now invoke the principle of stationary action and obtain the equation of motion in algebraic form. We vary the action integral with respect to $\psi_{\mu I}^*$ to obtain simultaneous equation for the coefficients $\psi_{\nu J}$,

$$\frac{\delta \mathcal{A}}{\delta \psi_{\mu I}^*} = \sum_{\nu} \sum_{J}^{n_{\text{glob}}} \mathcal{M}_{\mu\nu IJ} \psi_{\nu J} = 0. \tag{B8}$$

Given the particular form of the integrand in Eq. (B1), the above expression results in a generalized eigenvalue problem

$$\sum_{\nu} \sum_{J}^{n_{\text{glob}}} [\mathcal{H}_{\mu\nu IJ} - E\, \delta_{\mu\nu} \mathcal{S}_{\mu\nu IJ}] \psi_{\nu J} = 0. \tag{B9}$$

Here $\mathcal{H}_{\mu\nu IJ}$ represents the discretized form of the Burt-Foreman operator $\hat{H}_{BF}^{\mu\nu}$ in Eq. (2), while $\mathcal{S}_{\mu\nu IJ}$ is an overlap matrix which is present due to the nonorthogonality of the basis functions N_j. From Eq. (B9) it is clear that the dimension of the problem is given by the number of nodes n_{glob} in the simulation domain, times the number of components of the envelope function.

For the Poisson equation the energy functional to be minimized is given by

$$\mathcal{A} = \int \mathrm{d}\mathbf{r}_\perp \frac{1}{2} [\epsilon(\mathbf{r}_\perp)\, \nabla V_{el}(\mathbf{r}_\perp) \cdot \nabla V_{el}(\mathbf{r}_\perp) - \tfrac{1}{\epsilon_0} V_{el}(\mathbf{r}_\perp) \rho(\mathbf{r}_\perp)]. \tag{B10}$$

A functional variation of $\mathcal{A}$ with respect to V_{el} followed by an integration by parts gives the Poisson equation Eq. (7). Expressing the electrostatic potential again in terms of Lagrange linear interpolation polynomials inside each triangular element,

$$V_{el}(\mathbf{r}_\perp) = \sum_{j=1}^{3} V_{el}^j N_j(\mathbf{r}_\perp), \tag{B11}$$

and following the same procedure described for the $\mathbf{k} \cdot \mathbf{p}$ problem, a linear system of n_{glob} equations is obtained:

$$\sum_{J}^{n_{\text{glob}}} C_{IJ} V_{el}^J = b_I. \tag{B12}$$

After the inclusion of proper boundary conditions, Eqs. (B9) and (B12) are finally solved with standard library routines.

[1] C. Jia, Z. Lin, Y. Huang, and X. Duan, Nanowire electronics: From nanoscale to macroscale, Chem. Rev. **119**, 9074 (2019).

[2] Y. Zhang, J. Wu, M. Aagesen, and H. Liu, III–V nanowires and nanowire optoelectronic devices, J. Phys. D: Appl. Phys. **48**, 463001 (2015).

[3] C. Zhang and X. Li, III-V nanowire transistors for low-power logic applications: A review and outlook, IEEE Trans. Electron Devices **63**, 223 (2016).

[4] B. Mandl, J. Stangl, T. Ma, A. Mikkelsen, L. Samuelson, J. Eriksson, L. S. Karlsson, and W. Seifert, Au-free epitaxial growth of InAs nanowires, Nano Lett. **6**, 1817 (2006).

[5] S. Breuer, C. Pfüller, T. Flissikowski, O. Brandt, H. T. Grahn, L. Geelhaar, and H. Riechert, Suitability of Au- and self-assisted GaAs nanowires for optoelectronic applications, Nano Lett. **11**, 1276 (2011).

[6] P. Krogstrup, R. Popovitz-Biro, E. Johnson, M. H. Madsen, J. Nygård, and H. Shtrikman, Structural phase control in self-catalyzed growth of GaAs nanowires on silicon (111), Nano Lett. **10**, 4475 (2010).

[7] K. A. Dick, J. Bolinsson, M. E. Messing, S. Lehmann, J. Johansson, and P. Caroff, Parameter space mapping of InAs nanowire crystal structure, J. Vac. Sci. Technol. B **29**, 04D103 (2011).

[8] R. R. Zamani, F. S. Hage, S. Lehmann, Q. M. Ramasse, and K. A. Dick, Atomic-resolution spectrum imaging of semiconductor nanowires, Nano Lett. **18**, 1557 (2018).

[9] M. Royo, M. D. Luca, R. Rurali, and I. Zardo, A review on III – V core – multishell nanowires : growth, properties, and applications, J. Phys. D: Appl. Phys. **50**, 143001 (2017).

[10] D. Spirkoska, A. Fontcuberta i Morral, J. Dufouleur, Q. Xie, and G. Abstreiter, Free standing modulation doped core-shell GaAs/AlGaAs hetero-nanowires, Phys. Status Solidi RRL **5**, 353 (2011).

[11] S. Funk, M. Royo, I. Zardo, D. Rudolph, S. Morkötter, B. Mayer, J. Becker, A. Bechtold, S. Matich, M. Döblinger, M. Bichler, G. Koblmüller, J. J. Finley, A. Bertoni, G. Goldoni, and G. Abstreiter, High mobility one- and two-dimensional electron systems in nanowire-based quantum heterostructures, Nano Lett. **13**, 6189 (2013).

[12] N. I. Goktas, E. M. Fiordaliso, and R. R. Lapierre, Doping assessment in GaAs nanowires, Nanotechnology **29**, 234001 (2018).

[13] W. Kim, L. Güniat, A. Fontcuberta I Morral, and V. Piazza, Doping challenges and pathways to industrial scalability of III-V nanowire arrays, Appl. Phys. Rev. **8**, 011304 (2021).

[14] J. Jadczak, P. Plochocka, A. Mitioglu, I. Breslavetz, M. Royo, A. Bertoni, G. Goldoni, T. Smolenski, P. Kossacki, A. Kretinin

et al., Unintentional high-density p-type modulation doping of a GaAs/AlAs core–multishell nanowire, Nano Lett. **14**, 2807 (2014).

[15] R. Dingle, H. L. Störmer, A. C. Gossard, and W. Wiegmann, Electron mobilities in modulation-doped semiconductor heterojunction superlattices, Appl. Phys. Lett. **33**, 665 (1978).

[16] Y. J. Chung, K. A. Villegas Rosales, K. W. Baldwin, P. T. Madathil, K. W. West, M. Shayegan, and L. N. Pfeiffer, Ultra-high-quality two-dimensional electron systems, Nat. Mater. **20**, 632 (2021).

[17] L. Balaghi, S. Shan, I. Fotev, F. Moebus, R. Rana, T. Venanzi, R. Hübner, T. Mikolajick, H. Schneider, M. Helm, A. Pashkin, and E. Dimakis, High electron mobility in strained GaAs nanowires, Nat. Commun. **12**, 6642 (2021).

[18] A. Bertoni, M. Royo, F. Mahawish, and G. Goldoni, Electron and hole gas in modulation-doped GaAs/Al_{1-x} Ga_x As radial heterojunctions, Phys. Rev. B **84**, 205323 (2011).

[19] M. Royo, A. Bertoni, and G. Goldoni, Symmetries in the collective excitations of an electron gas in core-shell nanowires, Phys. Rev. B **89**, 155416 (2014).

[20] M. Royo, A. Bertoni, and G. Goldoni, Prediction of inelastic light scattering spectra from electronic collective excitations in GaAs/AlGaAs core-multishell nanowires, Phys. Rev. B **91**, 245303 (2015).

[21] Y. Ishikawa, Scanning tunneling microscopy and x-ray photoelectron spectroscopy studies of atomic level structure and Fermi level pinning on GaAs(110) surfaces grown by molecular beam epitaxy, J. Vac. Sci. Technol. B **16**, 2387 (1998).

[22] P. A. Alekseev, M. S. Dunaevskiy, G. E. Cirlin, R. R. Reznik, A. N. Smirnov, D. A. Kirilenko, V. Y. Davydov, and V. L. Berkovits, Unified mechanism of the surface Fermi level pinning in III-As nanowires, Nanotechnology **29**, 314003 (2018).

[23] F. Buscemi, M. Royo, G. Goldoni, and A. Bertoni, Tailoring the core electron density in modulation-doped core-multi-shell nanowires, Nanotechnology **27**, 195201 (2016).

[24] M. Royo, A. Bertoni, and G. Goldoni, Landau levels, edge states, and magnetoconductance in GaAs/AlGaAs core-shell nanowires, Phys. Rev. B **87**, 115316 (2013).

[25] M. Royo, C. Segarra, A. Bertoni, G. Goldoni, and J. Planelles, Aharonov-Bohm oscillations and electron gas transitions in hexagonal core-shell nanowires with an axial magnetic field, Phys. Rev. B **91**, 115440 (2015).

[26] S. Wu, K. Peng, S. Battiato, V. Zannier, A. Bertoni, G. Goldoni, X. Xie, J. Yang, S. Xiao, C. Qian, F. Song, S. Sun, J. Dang, Y. Yu, F. Beltram, L. Sorba, A. Li, B. bei Li, F. Rossella, and X. Xu, Anisotropies of the g-factor tensor and diamagnetic coefficient in crystal-phase quantum dots in InP nanowires, Nano Res. **12**, 2842 (2019).

[27] G. Goldoni, F. Rossi, E. Molinari, A. Fasolino, R. Rinaldi, and R. Cingolani, Valence band spectroscopy in V-grooved quantum wires, Appl. Phys. Lett. **69**, 2965 (1996).

[28] G. Goldoni, F. Rossi, E. Molinari, and A. Fasolino, Band structure and optical anisotropy in V-shaped and T-shaped semiconductor quantum wires, Phys. Rev. B **55**, 7110 (1997).

[29] V. V. Ravi Kishore, B. Partoens, and F. M. Peeters, Electronic structure and optical absorption of GaAs/Al_xGa_{1-x}As and Al_xGa_{1-x}As/GaAs core-shell nanowires, Phys. Rev. B **82**, 235425 (2010).

[30] V. V. R. Kishore, B. Partoens, and F. M. Peeters, Electronic structure of InAs/GaSb core-shell nanowires, Phys. Rev. B **86**, 165439 (2012).

[31] B. Lassen, M. Willatzen, R. Melnik, and L. L. Y. Voon, Electronic structure of free-standing InP and InAs nanowires, J. Mater. Res. **21**, 2927 (2006).

[32] M.-E. Pistol and C. E. Pryor, Band structure of core-shell semiconductor nanowires, Phys. Rev. B **78**, 115319 (2008).

[33] N. Luo, G. Liao, and H. Q. Xu, K.P Theory of freestanding narrow band gap semiconductor nanowires, AIP Adv. **6**, 125109 (2016).

[34] N. Luo, G.-Y. Huang, G. Liao, L.-H. Ye, and H. Xu, Band-inverted gaps in InAs/GaSb and GaSb/InAs core-shell nanowires, Sci. Rep. **6**, 38698 (2016).

[35] L. Ram-Mohan and K. Yoo, Wavefunction engineering of layered semiconductors: theoretical foundations, J. Phys.: Condens. Matter **18**, R901 (2006).

[36] P. Wójcik, A. Bertoni, and G. Goldoni, Tuning rashba spin-orbit coupling in homogeneous semiconductor nanowires, Phys. Rev. B **97**, 165401 (2018).

[37] P. Wójcik, A. Bertoni, and G. Goldoni, Enhanced rashba spin-orbit coupling in core-shell nanowires by the interfacial effect, Appl. Phys. Lett. **114**, 073102 (2019).

[38] P. Wójcik, A. Bertoni, and G. Goldoni, Anisotropy of the spin-orbit coupling driven by a magnetic field in inas nanowires, Phys. Rev. B **103**, 085434 (2021).

[39] R. Ram-Mohan and L. R. Ram-Mohan, *Finite Element and Boundary Element Applications in Quantum Mechanics* (Oxford University Press on Demand, Oxford, 2002), Vol. 5.

[40] G. Dhatt, E. Lefrançois, and G. Touzot, *Finite Element Method* (Wiley, New York, 2012).

[41] O. C. Zienkiewicz, R. L. Taylor, and J. Z. Zhu, *The Finite Element Method: Its Basis and Fundamentals* (Elsevier, Amsterdam, 2005).

[42] D. Prete, E. Dimaggio, V. Demontis, V. Zannier, M. J. Rodriguez-Douton, L. Guazzelli, F. Beltram, L. Sorba, G. Pennelli, and F. Rossella, Electrostatic control of the thermoelectric figure of merit in ion-gated nanotransistors, Adv. Funct. Mater. **31**, 2104175 (2021).

[43] I. Vurgaftman, J. R. Meyer, and L. R. Ram-Mohan, Band parameters for III-V compound semiconductors and their alloys, J. Appl. Phys. **89**, 5815 (2001).

[44] S. Adachi, *Properties of Semiconductor Alloys: Group-IV, III-V and II-VI Semiconductors* (Wiley, New York, 2009).

[45] G. Bastard, *Wave Mechanics Applied to sSemiconductor Heterostructures* (Les Ulis Cedex, France, 1990).

[46] F. Hecht, New development in freefem++, J. Numer. Math. **20**, 251 (2012).

[47] E. A. de Andrada e Silva, G. C. La Rocca, and F. Bassani, Spin-orbit splitting of electronic states in semiconductor asymmetric quantum wells, Phys. Rev. B **55**, 16293 (1997).

[48] D. C. Sorensen, Implicitly restarted arnoldi/lanczos methods for large scale eigenvalue calculations, in *Parallel Numerical Algorithms* (Springer, Dordrecht, 1997), pp. 119–165.

[49] R. B. Lehoucq, D. C. Sorensen, and C. Yang, *ARPACK Users' Guide: Solution of Large-Scale Eigenvalue Problems with Implicitly Restarted Arnoldi Methods* (SIAM, Philadelphia, 1998).

[50] Note that the convergence of the diagonalization is affected by the actual value of E_{search} [78]. For this reason, computational times can be further reduced by using the minimum (maximum)

conduction (valence) band eigenvalue at $E_n^{\min}(k_z)$ [$E_n^{\max}(k_z)$] as E_{search} for the next diagonalization at $k_z + \Delta k_z$.

[51] V. Eyert, A comparative study on methods for convergence acceleration of iterative vector sequences, J. Comput. Phys. **124**, 271 (1996).

[52] D. D. Johnson, Modified broyden's method for accelerating convergence in self-consistent calculations, Phys. Rev. B **38**, 12807 (1988).

[53] D. Vanderbilt and S. G. Louie, Total energies of diamond (111) surface reconstructions by a linear combination of atomic orbitals method, Phys. Rev. B **30**, 6118 (1984).

[54] C. G. Broyden, A class of methods for solving nonlinear simultaneous equations, Math. Comp. **19**, 577 (1965).

[55] E. Cuthill and J. McKee, Reducing the bandwidth of sparse symmetric matrices, in *Proceedings of the 1969 24th National Conference* (Association for Computing Machinery, New York, 1969), pp. 157–172.

[56] P. Virtanen, R. Gommers, T. E. Oliphant, M. Haberland, T. Reddy, D. Cournapeau, E. Burovski, P. Peterson, W. Weckesser, J. Bright, S. J. van der Walt, M. Brett, J. Wilson, K. J. Millman, N. Mayorov, A. R. J. Nelson, E. Jones, R. Kern, E. Larson, C. J. Carey *et al.*, SciPy 1.0: Fundamental Algorithms for Scientific Computing in Python, Nat. Methods **17**, 261 (2020).

[57] The SO component for these states is negligible and it is not shown here.

[58] G. Ferrari, G. Goldoni, A. Bertoni, G. Cuoghi, and E. Molinari, Magnetic states in prismatic core multishell nanowires, Nano Lett. **9**, 1631 (2009).

[59] I. Kokurin, Electronic states in nanowires with hexagonal cross-section, Semiconductors **54**, 1897 (2020).

[60] Note that the quantization axis of the total angular momentum **J** is chosen along the free direction, i.e., the nanowire axis z, not along the confinement direction, as usually done in quantum wells; hence the HH/LH labelling of the highest valence state is opposite to the quantum well case, see, e.g., Ref. [75].

[61] G. Liao, N. Luo, K.-Q. Chen, and H. Q. Xu, Electronic structures of free-standing nanowires made from indirect bandgap semiconductor gallium phosphide, Sci. Rep. **6**, 28240 (2016).

[62] G. Liao, N. Luo, K.-Q. Chen, and H. Q. Xu, Electronic structures of [1 1 1]-oriented free-standing InAs and InP nanowires, J. Phys.: Condens. Matter **28**, 135303 (2016).

[63] M. Cygorek, M. Korkusinski, and P. Hawrylak, Atomistic theory of electronic and optical properties of InAsP/InP nanowire quantum dots, Phys. Rev. B **101**, 075307 (2020).

[64] It should be noted that our $\mathbf{k}\cdot\mathbf{p}$ model has an higher symmetry with respect to an atomistic Hamiltonian due to lack of bulk inversion symmetry in III-V materials. This would remove the double degeneracy of our $\mathbf{k}\cdot\mathbf{p}$ subbands with tiny spin-splittings in the micro-eV range [62].

[65] A. Sitek, M. Urbaneja Torres, and A. Manolescu, Corner and side localization of electrons in irregular hexagonal semiconductor shells, Nanotechnology **30**, 454001 (2019).

[66] F. Rossi and E. Molinari, Coulomb-Induced Suppression of Band-Edge Singularities in the Optical Spectra of Realistic Quantum-Wire Structures, Phys. Rev. Lett. **76**, 3642 (1996).

[67] F. Rossi, G. Goldoni, O. Mauritz, and E. Molinari, Theory of excitonic confinement in semiconductor quantum wires, J. Phys.: Condens. Matter **11**, 5969 (1999).

[68] G. Goldoni and F. Rossi, Optimization of semiconductor quantum devices by evolutionary search, Opt. Lett. **25**, 1025 (2006).

[69] G. Goldoni, Optimal design and quantum limit for second harmonic generation in semiconductor heterostructures, J. Appl. Phys. **89**, 1755 (2001).

[70] S. Birner, The multi-band $\mathbf{k}\cdot\mathbf{p}$ hamiltonian for heterostructures: Parameters and applications, in *Multi-Band Effective Mass Approximations* (Springer, Cham, 2014), pp. 193–244.

[71] T. Eissfeller and P. Vogl, Real-space multiband envelope-function approach without spurious solutions, Phys. Rev. B **84**, 195122 (2011).

[72] B. A. Foreman, Elimination of spurious solutions from eight-band $\mathbf{k}\cdot\mathbf{p}$ theory, Phys. Rev. B **56**, R12748 (1997).

[73] R. G. Veprek, S. Steiger, and B. Witzigmann, Ellipticity and the spurious solution problem of $\mathbf{k}\cdot\mathbf{p}$ envelope equations, Phys. Rev. B **76**, 165320 (2007).

[74] B. A. Foreman, Choosing a basis that eliminates spurious solutions in $\mathbf{k}\cdot\mathbf{p}$ theory, Phys. Rev. B **75**, 235331 (2007).

[75] J. Los, A. Fasolino, and A. Catellani, Generalization of the k·p approach for strained layered semiconductor structures grown on high-index-planes, Phys. Rev. B **53**, 4630 (1996).

[76] J. C. Yi and N. Dagli, Finite-element analysis of valence band structure and optical properties of quantum-wire arrays on vicinal substrates, IEEE J. Quantum Electron. **31**, 208 (1995).

[77] M. Ogawa, T. Kunimasa, T. Ito, and T. Miyoshi, Finite-element analysis of quantum wires with arbitrary cross sections, J. Appl. Phys. **84**, 3242 (1998).

[78] T. Andlauer, Optoelectronic and spin-related properties of semiconductor nanostructures in magnetic fields, Ph.D. thesis, Technische Universität München, 2009.

Correction: The previously published Figures 2, 5, 8, 10, and 11 contained incorrect x-axis values and have been replaced. Minor errors in Eqs. (A4), (A6), (A19), (B9), and in an inline equation above Eq. (A6) have been fixed.